

Highlights

PVD-ONet: A Multi-scale Neural Operator Method for Singularly Perturbed Boundary Layer Problems

Tiantian Sun, Jian Zu

- PVD-Net: a physics-informed framework for singularly perturbed problems.
- PVD-ONet: an operator-learning model for a family of boundary layer problems.
- Van Dyke matching principle is introduced to enhance prediction accuracy.
- Model design embeds perturbation theory, providing strong interpretability.
- Numerical results show our methods exceed baseline performance.

PVD-ONet: A Multi-scale Neural Operator Method for Singularly Perturbed Boundary Layer Problems

Tiantian Sun^a, Jian Zu^{a,*}

^a*School of Mathematics and Statistics, Center for Mathematics and Interdisciplinary Sciences, Northeast Normal University, Changchun 130024, P.R. China*

Abstract

Physics-informed neural networks and Physics-informed DeepONet excel in solving partial differential equations; however, they often fail to converge for singularly perturbed problems. To address this, we propose two novel frameworks, *Prandtl-Van Dyke neural network* (PVD-Net) and its operator learning extension *Prandtl-Van Dyke Deep Operator Network* (PVD-ONet), which rely solely on governing equations without data. To address varying task-specific requirements, both PVD-Net and PVD-ONet are developed in two distinct versions, tailored respectively for stability-focused and high-accuracy modeling. The leading-order PVD-Net adopts a two-network architecture combined with Prandtl's matching condition, targeting stability-prioritized scenarios. The high-order PVD-Net employs a five-network design with Van Dyke's matching principle to capture fine-scale boundary layer structures, making it ideal for high-accuracy scenarios. PVD-ONet generalizes PVD-Net to the operator learning setting by assembling multiple DeepONet modules, directly mapping initial conditions to solution operators and enabling instant predictions for an entire family of boundary layer problems without retraining. Numerical experiments on various models show that our proposed methods consistently outperform existing baselines under various error metrics, thereby offering a powerful new approach for multi-scale problems.

Keywords: Singularly perturbed problem; Matched asymptotic expansions; Machine learning; Operator learning; Multi-scale problem

1. Introduction

Singular perturbation problems are prevalent in various scientific and engineering disciplines, including fluid mechanics [1, 2], aerodynamics [3, 4, 5], solid mechanics [6, 7, 8], and biological transport [9]. For example, in aerodynamics, singular perturbation methods are used to analyze rapid pressure and velocity changes around a thin airfoil. Such problems typically involve a small parameter multiplying the highest-order derivative in the differential equations [10], resulting in abrupt changes in the solution within localized

*Corresponding author

Email address: zuj100@nenu.edu.cn (Jian Zu)

regions. This leads to multi-scale phenomena and often forms boundary layer structures. In 1904, Prandtl [11] proposed the boundary layer theory, which effectively addressed the singular perturbation difficulties and laid the theoretical foundation for calculating aerodynamic drag and lift in aircraft design. In 1921, von Kármán [12] derived the boundary layer momentum integral equation, further advancing the experimental and engineering applications of the theory. In 1962, Van Dyke [13, 14, 15] systematically developed a high-order matching method for boundary layer problems, providing a theoretical foundation for constructing accurate high-order approximations. O'Malley [16, 17, 18, 19] has made fundamental contributions to the theory of singular perturbations and boundary layer analysis, particularly in the context of differential equations with multiple small parameters and nonlinear initial value problems. Nayfeh's seminal work [10, 20, 21, 22] provided a rigorous foundation for treating singular perturbation problems, which has greatly influenced subsequent developments in boundary layer theory and nonlinear dynamics. To solve these boundary layer problems, traditional and widely used mesh-based numerical methods, such as the Finite Element Method (FEM) [23], Finite Volume Method (FVM) [24], and Finite Difference Method (FDM) [25], are commonly employed. However, these methods often require fine meshes to resolve multiscale phenomena and provide only numerical approximations without explicit analytical structure. In contrast, the singular perturbation methods are mesh-free and offers near-analytical solutions, directly capturing the problem's inherent behavior without the need for mesh refinement. As a result, singular perturbation methods have consistently attracted considerable attention in the science and engineering fields.

In recent years, the rapid advancement of artificial intelligence has sparked growing interest in deep learning methods among researchers. Researchers have begun exploring Scientific Machine Learning (SciML) as an alternative to traditional numerical methods for complex system modeling [26, 27, 28, 29]. Physics-Informed Neural Networks (PINNs) [30, 31] incorporate governing equations as soft constraints within the loss function, enabling the neural network to naturally satisfy the underlying physical laws. This approach enhances generalization, reduces reliance on labeled data, and provides an effective framework for solving differential equations. PINNs have been successfully applied to a wide range of problems across various fields, including biology research [32], chemical kinetics [33], fluid mechanics [34, 35, 36] and material science [37], among others. However, PINNs encounter convergence difficulties when applied to multi-scale problems [38]. Existing literature [39] indicates that this issue persists even with the application of advanced techniques, such as domain decomposition [40] and importance sampling [41], commonly employed to enhance convergence. This challenge may stem from the inability of a single PINNs to simultaneously capture variations across different scales when addressing multi-scale problems [42]. From the perspective of approximating analytical solutions, perturbation techniques exhibit a natural connection with deep learning methods, offering a promising pathway to address the aforementioned challenges. Since the method of matched asymptotic expansions is a classical approach for handling multi-scale problems in singular perturbation theory [10, 13, 14, 15, 43], a natural idea is to combine it with the PINNs framework. Notably,

unlike traditional perturbation approaches requiring intricate derivations, combining matched asymptotic expansions with PINNs eliminates the need for manual analysis while retaining the advantage of operating directly on the governing equations under perturbation theory.

Recent works have started exploring hybrid approaches that integrate matched asymptotic expansions with PINNs to better model singularly perturbed problems. Arzani et al. proposed Boundary-layer PINNs (BL-PINNs) [39], which employ two separate neural networks to approximate the inner and outer solutions. These solutions are then connected through the Prandtl matching principle to obtain the leading-order approximate solution. However, their piecewise formulation may lead to reduced accuracy in transition regions. Zhang and He [44] proposed the Multi-Scale-Matching Neural Networks (MSM-NN) framework to address problems with multiple boundary layers. By introducing exponential stretched variables in the boundary layers, their method avoids semi-infinite domain issues and improves solution accuracy. Other works [45, 46] have combined asymptotic expansions with PINNs, but they primarily focus on leading-order approximations and struggle to capture higher-order effects, limiting their ability to achieve high-accuracy solutions. The application of higher-order matching techniques, such as Van Dyke matching [13, 14, 15], to multi-scale problems remains largely unexplored.

In this paper, our first contribution is the proposal of the Prandtl-Van Dyke neural network (PVD-Net), a novel deep learning framework for solving boundary layer problems, which consists of a leading-order PVD-Net and a high-order PVD-Net. For leading-order PVD-Net, two neural networks are used to learn the inner and outer solutions separately. By constructing a global composite solution through the Prandtl matching principle, we obtain a uniformly valid approximation—this is the crucial feature that significantly enhances numerical accuracy of BL-PINNs in the transition region. For high-order PVD-Net, we propose a novel five-network architecture incorporating Van Dyke’s matching principle. This framework systematically captures finer-scale variations through higher-order asymptotic matching, enabling significantly improved numerical accuracy compared to leading-order PVD-Net.

The second contribution of our work is the proposal of Prandtl-Van Dyke Deep Operator Network (PVD-ONet), an innovative operator learning framework for addressing a family of boundary layer problems. Inspired by the core idea of PVD-Net, the PVD-ONet framework similarly comprises two components: the leading-order PVD-ONet and the high-order PVD-ONet. PVD-Net enables fast training and efficient solution of boundary layer problems under fixed settings. However, it is typically tailored to specific cases, requiring network retraining when system parameters (e.g., initial value conditions, boundary conditions, etc.) change. In order to break through this limitation, we have gradually turned our attention to more generalized operator learning methods [47, 48, 49, 50]. Unlike PINNs, operator learning directly maps input spaces (e.g., initial and boundary conditions) to output spaces (e.g., solution fields), enabling the modeling of infinite-dimensional spaces. Neural operators approximate solution operators parametrically, learning entire PDE families in a single training process and allowing fast online inference for new instances while

significantly reducing computational cost. Researchers have proposed advanced neural operator architectures, with the Fourier Neural Operator (FNO) [49] and Deep Operator Network (DeepONet) [48] being among the most notable. FNO discretizes both the input and output spaces on a fixed, equispaced mesh and learns solution operators in the Fourier domain to capture global dependencies in function space. DeepONet employs a branch-trunk architecture to approximate nonlinear operators, where the branch network encodes the input function at sensor locations while the trunk network evaluates the output at target coordinates. Li et al. [51] proposed the use of DeepONet to learn the solutions of a family of boundary layer problems, allowing the method to adapt to different initial conditions without retraining the network. However, despite the impressive performance of these methods, they are predominantly used in a data-driven manner. Typically, due to the extremely thin structure of boundary layers, obtaining high-fidelity measurement data is exceedingly difficult and often infeasible in practice. For instance, in high-speed aerodynamics, the viscous boundary layer formed over the surface of a supersonic aircraft can be as thin as a few hundred micrometers. Wang et al. [52] proposed the Physics-informed DeepONet (PI-DeepONet) method, which integrates physical constraints into the DeepONet framework. This approach reduces the reliance on expensive high-fidelity data by enforcing physical constraints, making it more feasible to train models with limited data. However, for multi-scale problems, PI-DeepONet still encounters convergence issues and struggles to capture the sharp transitions in the solution. Learning the solutions of a family of boundary layer problems based solely on equation information remains largely unexplored in current research. Thus, our proposed PVD-ONet fills this gap by extending the core idea of PVD-Net to the operator learning framework. The leading-order PVD-ONet inherits the two-network architecture from PVD-Net, utilizing two DeepONet models to separately approximate the inner and outer solutions, which are then connected through Prandtl’s matching conditions. Additionally, we introduce a composite solution to obtain the solution across the entire domain. For high-order PVD-ONet, we extend the paradigm of high-order PVD-Net by employing five DeepONet models to more accurately learn the solution of the boundary layer problem, achieving greater precision compared to the leading-order approximation. By incorporating the Van Dyke matching principle, we effectively connect solutions from different regions. A detailed comparison of neural network-based methods for boundary layer approximation is provided (see Table 1). The contributions of this work can be summarized as follows:

- We propose PVD-Net to address the limitations of PINNs in multi-scale problems. For leading-order approximations, we enhance BL-PINNs by incorporating a composite solution in the transition regions, significantly improving accuracy while ensuring stability and efficiency. For higher-order approximations, we incorporate five neural networks with Van Dyke matching, enabling high-accuracy learning of fine-scale solution structures.
- We propose PVD-ONet, which advances PVD-Net by incorporating operator learning to solve a family

of boundary layer problems. Like PVD-Net, it offers both leading- and high-order approximations. By leveraging operator learning, PVD-ONet enables fast, accurate predictions for new inputs via a single forward pass, eliminating retraining and supporting efficient online deployment.

- Our methods rely solely on equation information, eliminating the need for additional data in neural network training. This effectively bypasses the challenges of acquiring high-fidelity data for boundary layer problems, maintaining physical fidelity without relying on hard-to-obtain measurements.
- By embedding singular perturbation theory into the model design, our proposed frameworks offer theoretically grounded interpretability and captures the intrinsic multi-scale nature of boundary layer problems.
- We performed direct comparisons with other state-of-the-art methods. The experimental results demonstrate that our leading-order approximation outperforms the baseline, and our high-order approximation achieves higher accuracy than the leading-order approximation. The high-order version offers additional accuracy benefits for applications demanding finer accuracy.

Table 1: Comparison of neural network-based methods for boundary layer approximation.

Method	Training Speed	New Instance Inference	Leading-Order Approximation	High-Order Approximation	Smooth Solution
BL-PINNs	Fast	No	Yes	No	No
MSM-NN	Fast	No	Yes	No	Yes
PVD-Net (Ours)	Fast	No	Yes (Stable, Simple)	Yes (High Precision)	Yes
PVD-ONet (Ours)	Slow	Yes	Yes (Stable, Simple)	Yes (High Precision)	Yes

The remainder of this paper is organized as follows. In Section 2, we present the formulation of singular perturbation problems and introduce the method of matched asymptotic expansions. Section 3 details the proposed PVD-Net and PVD-ONet frameworks. Numerical experiments are conducted in Section 4 to validate the effectiveness of our approach. Finally, Section 5 concludes the paper and outlines potential directions for future research.

2. Problem Setup and Matched Asymptotic Expansion Techniques

2.1. Problem Statement

Perturbation methods are commonly used to analyze differential equations containing a small parameter $\varepsilon \ll 1$. It can generally be classified into two types: regular and singular perturbations. In regular perturbation problems, the solution varies smoothly with respect to ε , and setting $\varepsilon = 0$ yields a reduced problem

whose solution remains a good approximation throughout the entire domain. However, many problems of practical importance fall into the category of singular perturbation problems, where the small parameter ε multiplies the highest-order derivative in the differential equation. These problems are particularly challenging because the solution behavior for $\varepsilon = 0$ differs fundamentally from the behavior as $\varepsilon \rightarrow 0$. This discrepancy gives rise to sharp gradients or boundary layers, making the construction of accurate approximations considerably more difficult than in regular perturbation problems.

Consider a differential equation of the following form:

$$\mathcal{F}(u, x, \varepsilon) = 0, \quad x \in \Omega \subseteq \mathbb{R}^n, \quad (1)$$

which subjects to suitable boundary conditions,

$$\mathcal{B}(u, \varepsilon) = 0 \quad \text{on} \quad \partial\Omega, \quad (2)$$

where $\varepsilon \ll 1$ is the small parameter, $u : \Omega \rightarrow \mathbb{R}$ is the unknown solution of equation (1), $\mathcal{B}(u, \varepsilon)$ represents boundary conditions such as Dirichlet, Neumann, and so on, depending on the specific problem. We consider an asymptotic expansion of the unknown solution $u(x; \varepsilon)$ in powers of the small parameter ε :

$$u(x; \varepsilon) = u_0(x) + \varepsilon u_1(x) + \varepsilon^2 u_2(x) + \cdots.$$

In regular perturbation problems, substituting this expansion into the original equation (1) and matching terms at each order of ε typically yields a sequence of well-posed problems for u_0, u_1, u_2, \dots , valid uniformly across the entire domain.

However, when the small parameter ε multiplies the highest-order derivative term, the regular perturbation method breaks down, and the problem falls into the category of singular perturbation problems, which are notably more challenging due to the presence of boundary layers and the failure of uniform asymptotic expansions. In such cases, directly setting $\varepsilon = 0$ typically reduces the order of the differential equation, which results in redundant boundary conditions and leads to an ill-posed problem. A prominent feature of this type of problem is the appearance of boundary layers, where the solution exhibits abrupt changes in certain local regions, while in the remaining regions, the solution changes relatively smoothly. The thickness of the boundary layer is usually related to ε . As $\varepsilon \rightarrow 0$, the boundary layer becomes extremely narrow. This phenomenon makes it difficult for conventional regular asymptotic expansion methods to effectively describe the global behavior of the solution. To overcome this difficulty, multi-scale analysis needs to be introduced, particularly the method of matched asymptotic expansion.

2.2. Matched Asymptotic Expansion

For region $\Omega_o \subset \Omega$ away from the boundary layer, the outer expansion of the solution is defined as:

$$u^o(x; \varepsilon) = \sum_{k=0}^{\infty} \varepsilon^k \varphi_k(x),$$

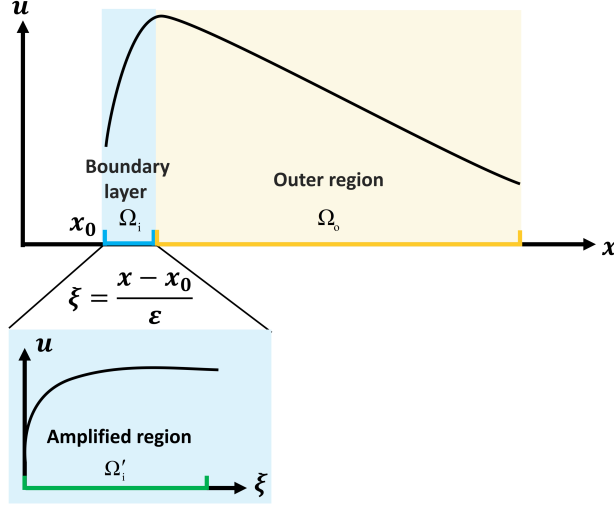


Figure 1: Schematic diagram of the boundary layer scale transformation. The diagram illustrates the evolution of the boundary layer's scale. The domain is decomposed into two parts: a boundary layer region Ω_i and an outer region Ω_o . By introducing the transformation $\xi = \frac{x-x_0}{\varepsilon}$, the boundary layer region Ω_i is mapped to an amplified region Ω'_i in the stretched coordinate.

where $\varphi_k : \Omega_o \rightarrow \mathbb{R}$ represents the asymptotic solutions for each scale in the region Ω_o . By substituting the outer expansion $u^o(x; \varepsilon)$ into (1), the governing equation becomes

$$\mathcal{F}_0(\varphi_0, x) + \varepsilon \mathcal{F}_1(\varphi_0, \varphi_1, x) + \varepsilon^2 \mathcal{F}_2(\varphi_0, \varphi_1, \varphi_2, x) + \cdots = 0,$$

where \mathcal{F}_k ($k = 0, 1, 2, \dots$) are differential operators arising from the expansion of \mathcal{F} . According to the theory of singular perturbations, the outer solution satisfies only the boundary conditions on the outer boundary and ignores the conditions near the boundary layer, i.e.,

$$\mathcal{B}^o(u^o, \varepsilon) = 0.$$

For the boundary layer region Ω_i , a new stretched variable $\xi = \frac{x-x_0}{\varepsilon^\lambda} \in \Omega'_i$ needs to be introduced to amplify the boundary layer, where x_0 is the location of the boundary layer. In this paper, for convenience, we set the stretching exponent $\lambda = 1$, and the choice of scaling will be discussed in another paper. A schematic diagram of the boundary layer scale transformation is shown in Figure 1. The rescaling of the original equation (1) leads to a new form of the equation in terms of ξ . Specifically, after applying the stretching transformation, the governing equation becomes

$$\tilde{\mathcal{F}}(u, \xi, \varepsilon) = 0, \tag{3}$$

where $\tilde{\mathcal{F}}$ represents the transformed operator, with derivatives taken with respect to ξ instead of x . The new equation describes the behavior of the solution in the boundary layer region. Next, the solution in the

boundary layer can be expressed as an asymptotic expansion in ε as follows:

$$u^i(\xi; \varepsilon) = \sum_{k=0}^{\infty} \varepsilon^k \psi_k(\xi),$$

where $\psi_k : \Omega'_i \rightarrow \mathbb{R}$ are coefficient functions that describe the behavior of the solution in the boundary layer region. Substituting this expansion into the rescaled equation (3), we obtain the following asymptotic expansion of the operator $\tilde{\mathcal{F}}$:

$$\tilde{\mathcal{F}}_0(\psi_0, \xi) + \varepsilon \tilde{\mathcal{F}}_1(\psi_0, \psi_1, \xi) + \varepsilon^2 \tilde{\mathcal{F}}_2(\psi_0, \psi_1, \psi_2, \xi) + \cdots = 0,$$

where $\tilde{\mathcal{F}}_k$ ($k = 0, 1, 2, \dots$) are the differential operators that arise from the expansion of $\tilde{\mathcal{F}}$. The inner solution satisfies only the boundary conditions within the boundary layer region, i.e.,

$$\mathcal{B}^i(u^i, \varepsilon) = 0.$$

Asymptotic solutions in different regions are connected via matching techniques to ensure a uniformly valid approximation over the entire domain. Prandtl's matching principle [11] effectively matches leading-order inner and outer solutions. For higher-order approximations in singular perturbation problems, the Van Dyke matching method [13, 14, 15] is used, allowing more accurate composite solutions by ensuring consistency in higher-order expansions. Specifically, the principles are as follows:

Prandtl Matching Principle [10]. The outer limit of the inner solution is equal to the inner limit of the outer solution.

Van Dyke Matching Principle [10]. The m -term inner expansion of the n -term outer expansion is equal to the n -term outer expansion of the m -term inner expansion, where m, n are arbitrary integers.

Finally, we can construct a single solution that is uniformly valid across the entire domain, known as the composite solution [10, 53], i.e.,

$$u^c(x) = u^i\left(\frac{x-x_0}{\varepsilon}\right) + u^o(x) - u^{o,i}, \quad x \in \Omega,$$

where $u^{o,i}$ denotes the Prandtl matching term or the Van Dyke matching term.

Remark 1. Although the inner solution $u^i\left(\frac{x-x_0}{\varepsilon}\right)$ is formally defined in the inner region Ω_i , it decays rapidly to the matching term $u^{o,i}$ outside this region and thus can be smoothly extended to the entire domain Ω . Similarly, the outer solution $u^o(x)$ is originally defined in the outer region Ω_o , but it can be smoothly extrapolated into the inner region. The matching term $u^{o,i}$ serves to remove the overlapping contribution, ensuring that the composite solution remains uniformly valid across the whole domain Ω .

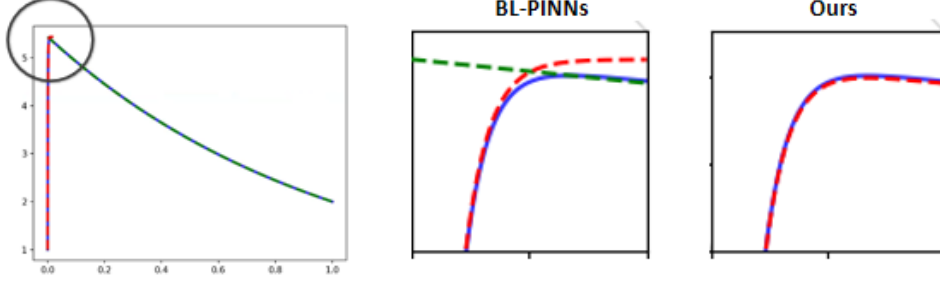


Figure 2: Comparison of predicted results in the boundary layer region between our method and the baseline (BL-PINNs), using the representative boundary layer problem $\varepsilon u'' + u' + u = 0$ as an example. **(Left)**: Global prediction results of BL-PINNs. The blue solid line represents the analytical solution; the red dashed line indicates the predicted inner solution, and the green dashed line indicates the predicted outer solution. **(Middle)**: Localized enlarged view of BL-PINNs in the boundary layer region, which shows a significant accuracy loss in the transition region. **(Right)**: A localized zoomed-in view of our method (blue solid line: analytical solution; red dashed line: predicted solution). It can be seen that our method is able to realize smooth transitions and significantly improve the accuracy.

The introduction of the composite solution significantly improves the accuracy in the transition region between the inner and outer layers, mitigating the loss of precision. To illustrate this improvement, we take the following representative boundary layer problem as an example:

$$\begin{cases} \varepsilon \frac{d^2 u}{dx^2} + \frac{du}{dx} + u = 0, & x \in (0, 1), \\ u(0) = \alpha, & u(1) = \beta, \end{cases}$$

where $\varepsilon = 10^{-3}$, $\alpha = 1$ and $\beta = 2$. As shown in Figure 2, the composite solution exhibits significantly improved accuracy compared to other method.

3. Methods

3.1. Prandtl-Van Dyke Neural Network (PVD-Net)

In this section, we provide a detailed description of PVD-Net. PVD-Net consists of two components, each tailored for different goals. It is worth emphasizing that our method is directly based on the governing equations and does not require any complicated analytical derivations. The leading-order PVD-Net leverages Prandtl matching to construct a robust leading-order approximation, which is particularly suitable for scenarios where stability and computational efficiency are prioritized. In contrast, the high-order PVD-Net employs Van Dyke matching to match and retain higher-order asymptotic terms, making it well-suited for applications that demand higher accuracy. This dual-level design ensures that PVD-Net can flexibly adapt to a wide range of modeling needs, balancing stability and precision. The architecture of the PVD-Net is illustrated in Figure 3.

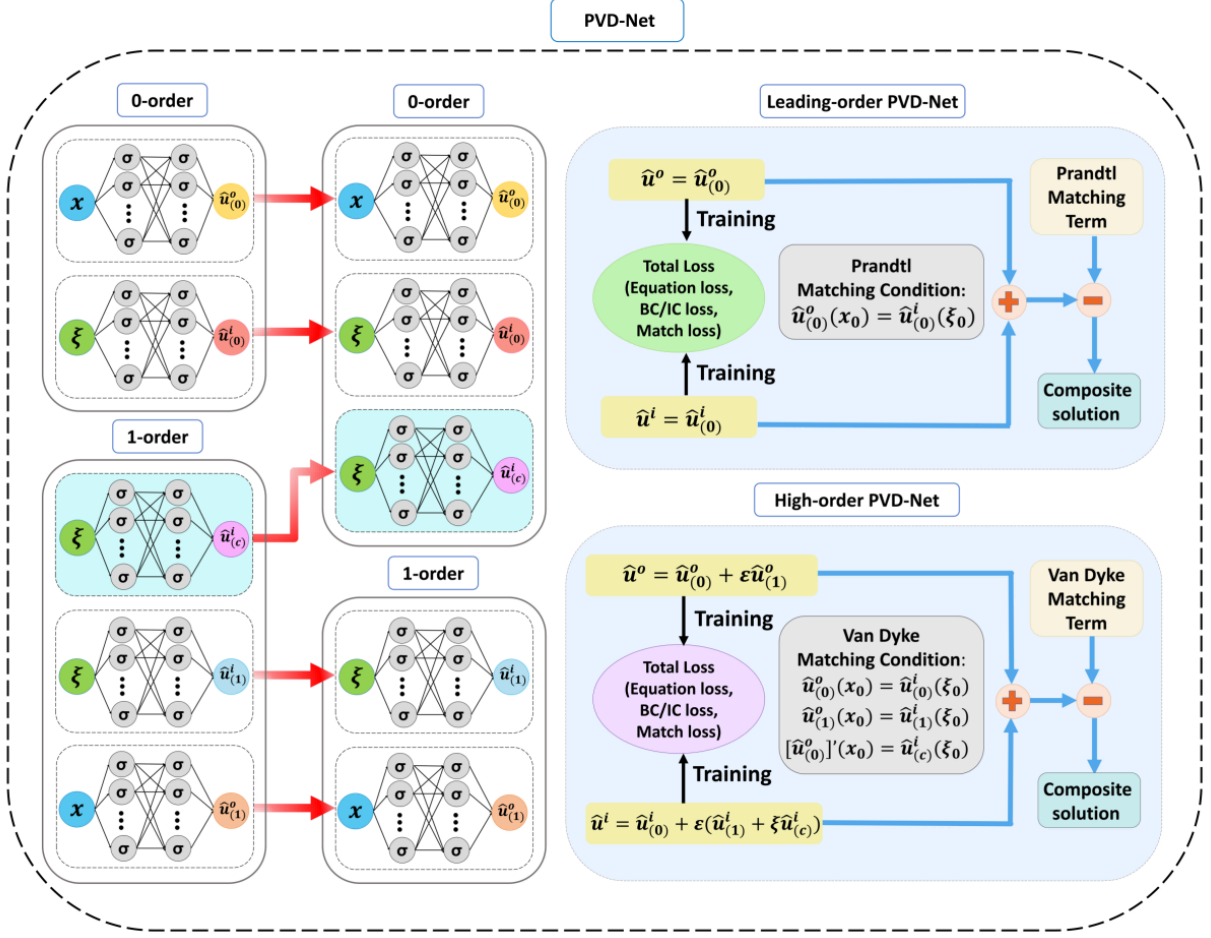


Figure 3: The network architecture of PVD-Net. The PVD-Net consists of two distinct configurations: a leading-order version and a higher-order version. The leading-order PVD-Net employs two neural networks—an outer network and an inner network—to solve boundary layer problems through Prandtl’s matching conditions, with the loss function computed accordingly. For the higher-order PVD-Net, the framework utilizes five neural networks in a hierarchical manner: two networks are dedicated to the zeroth-order approximation, while three networks handle the first-order approximation. This novel architecture implements the Van Dyke matching principle to achieve asymptotic matching between solutions of different orders, with the loss function computed accordingly. Notably, within this architecture, one of the first-order approximation networks naturally reduces to the zeroth-order case, maintaining consistency across approximation orders. Finally, both leading-order and high-order PVD-Net use composite solutions to obtain the output, thus guaranteeing smooth transitions in the solution.

3.1.1. Leading-order PVD-Net

For the leading-order PVD-Net, we employ a fully connected neural network $\hat{u}_{(0)}^o(x; \theta_1)$ as a surrogate model for the outer solution of (1). Similarly, another fully connected neural network $\hat{u}_{(0)}^i(\xi; \theta_2)$ is used to represent the inner solution. Here x is the outer variable, $\xi = \frac{x-x_0}{\varepsilon}$ is the stretched inner variable, θ_1, θ_2 are the trainable parameter. We simplify notation by writing $\hat{u}_{(0)}^o(x)$ and $\hat{u}_{(0)}^i(\xi)$ for $\hat{u}_{(0)}^o(x; \theta_1)$ and $\hat{u}_{(0)}^i(\xi; \theta_2)$,

respectively, whenever no confusion arises. The Prandtl matching principle can be denoted by

$$\lim_{x \rightarrow x_0} \hat{u}_{(0)}^o(x) = \lim_{\xi \rightarrow \infty} \hat{u}_{(0)}^i(\xi).$$

As computers are incapable of handling infinity, we approximate it by choosing a sufficiently large but finite value ξ_0 . This is justified by the fact that the inner solution decays exponentially in the outer region, so choosing a sufficiently large ξ_0 yields the same effect as taking $\xi \rightarrow \infty$.

Let $\mathcal{T} = \mathcal{T}_o \cup \mathcal{T}_i \cup \mathcal{T}_m \cup \mathcal{T}_b$, where $\mathcal{T}_o \subset \Omega_o$ and $\mathcal{T}_i \subset \Omega'_i$ are finite sets of residual points sampled from their respective domains, respectively. The set $\mathcal{T}_b = \Gamma^i \cup \Gamma^o$ consists of boundary residual points, with $\Gamma^i := \partial\Omega \setminus \partial\Omega_o$, $\Gamma^o := \partial\Omega \setminus \partial\Omega_i$. $\mathcal{T}_m = \{x_0, \xi_0\}$ denotes the matching points under the matching principle. The neural networks are optimized by the following loss function:

$$\mathcal{L}(\theta; \mathcal{T}) := \mathcal{L}^o(\theta_1; \mathcal{T}_o) + \mathcal{L}^i(\theta_2; \mathcal{T}_i) + \mathcal{L}^m(\theta_1, \theta_2; \mathcal{T}_m) + \mathcal{L}^b(\theta_1, \theta_2; \mathcal{T}_b), \quad (4)$$

where

$$\mathcal{L}^o(\theta_1; \mathcal{T}_o) = \frac{1}{|\mathcal{T}_o|} \sum_{x \in \mathcal{T}_o} \left| \mathcal{F}_0(\hat{u}_{(0)}^o, x) \right|^2, \quad (5)$$

$$\mathcal{L}^i(\theta_2; \mathcal{T}_i) = \frac{1}{|\mathcal{T}_i|} \sum_{\xi \in \mathcal{T}_i} \left| \tilde{\mathcal{F}}_0(\hat{u}_{(0)}^i, \xi) \right|^2, \quad (6)$$

$$\mathcal{L}^m(\theta_1, \theta_2; \mathcal{T}_m) = \left| \hat{u}_{(0)}^o(x_0) - \hat{u}_{(0)}^i(\xi_0) \right|^2, \quad (7)$$

$$\mathcal{L}^b(\theta_1, \theta_2; \mathcal{T}_b) = \frac{1}{|\Gamma^o|} \sum_{x \in \Gamma^o} \left| \mathcal{B}^o(\hat{u}_{(0)}^o, \varepsilon) \right|^2 + \frac{1}{|\Gamma^i|} \sum_{\xi \in \Gamma^i} \left| \mathcal{B}^i(\hat{u}_{(0)}^i, \varepsilon) \right|^2. \quad (8)$$

Here $|\mathcal{T}_o|$, $|\mathcal{T}_i|$, $|\Gamma^o|$, and $|\Gamma^i|$ denote the size of the corresponding sets, and $\theta = \{\theta_1, \theta_2\}$. Automatic differentiation [54] is employed to compute the differential operators in the loss function (4), and the optimal parameters are obtained by minimizing the loss function:

$$\theta = \arg \min_{\theta} \mathcal{L}(\theta; \mathcal{T}).$$

This problem is typically addressed using gradient-based optimization algorithms such as ADAM [55] or L-BFGS [56].

After training the neural networks, in order to obtain a uniformly valid solution, we use a composite solution of the form

$$\hat{u}(x; \theta) = \hat{u}_{(0)}^o(x) + \hat{u}_{(0)}^i \left(\frac{x - x_0}{\varepsilon} \right) - \hat{u}_{(0)}^{o,i}, \quad x \in \Omega, \quad (9)$$

where $\hat{u}_{(0)}^{o,i} = \hat{u}_{(0)}^o(x_0)$ (or $\hat{u}_{(0)}^i(\xi_0)$) is the Prandtl matching term. Although the inner solution $\hat{u}_{(0)}^i(\frac{x-x_0}{\varepsilon})$ is defined in the inner region Ω_i , it decays rapidly to $u_{(0)}^{o,i}$ outside this region and can be smoothly extended to Ω . Likewise, the outer solution $\hat{u}_{(0)}^o(x)$ can be smoothly extrapolated into the inner region. The matching term $u_{(0)}^{o,i}$ eliminates the overlapping contribution, ensuring the composite solution remains uniformly valid across the domain. An algorithm for implementation of the proposed leading-order PVD-Net is provided in Algorithm 1.

Algorithm 1 Leading-order PVD-Net

- 1: **Input:** Outer residual points \mathcal{T}_o , inner residual points \mathcal{T}_i , matching points \mathcal{T}_m , boundary residual points \mathcal{T}_b , learning rate η , total iterations N_{iter} .
 - 2: **Output:** The trainable parameters θ , the composite solution $\hat{u}(x; \theta)$.
 - 3: Initialize outer network $\hat{u}_{(0)}^o(x; \theta_1)$ and inner network $\hat{u}_{(0)}^i(\xi; \theta_2)$;
 - 4: **for** $iter = 1$ to N_{iter} **do**
 - 5: Compute losses $\mathcal{L}^o, \mathcal{L}^i, \mathcal{L}^m, \mathcal{L}^b$ as defined in (5) – (8);
 - 6: Compute total loss $\mathcal{L}(\theta; \mathcal{T})$ as given in (4);
 - 7: Simultaneously update network parameters using gradient descent
 - 8: $\theta \leftarrow \theta - \eta \nabla_{\theta} \mathcal{L}$;
 - 9: **end for**
 - 10: Compute composite solution $\hat{u}(x; \theta)$ as given in (9);
 - 11: **Return** trained parameters θ ; composite solution $\hat{u}(x; \theta)$.
-

3.1.2. High-order PVD-Net

The leading-order PVD-Net is suitable for scenarios that prioritize stability. In contrast, Van Dyke’s matching principle accommodates higher-order asymptotic terms, enabling significantly improved solution accuracy when such precision is required. To this end, we propose the high-order PVD-Net, which incorporates Van Dyke’s matching principle to capture higher-order effects more accurately.

Assuming the governing equation is second-order, and in light of resonance phenomena, we employ five fully connected neural networks to construct a high-order surrogate for the solution to Equation (1). Specifically, $\hat{u}_{(0)}^o(x; \theta_1)$ and $\hat{u}_{(0)}^i(\xi; \theta_2)$ correspond to the zeroth-order approximations, while $\hat{u}_{(1)}^o(x; \theta_3)$, $\hat{u}_{(c)}^i(\xi; \theta_4)$, and $\hat{u}_{(1)}^i(\xi; \theta_5)$ are used to model the first-order approximations. Similarly, we simplify notation by using $\hat{u}_{(0)}^o(x)$ and $\hat{u}_{(0)}^i(\xi)$ for the zeroth-order approximations, and $\hat{u}_{(1)}^o(x)$, $\hat{u}_{(c)}^i(\xi)$, and $\hat{u}_{(1)}^i(\xi)$ for the first-order approximations, whenever the parameter dependence is clear from context. We propose a novel construction of the two-term asymptotic expansions for both the inner and outer solutions, which can be expressed as:

$$\begin{aligned}\hat{u}^o(x; \theta_1, \theta_3) &= \hat{u}_{(0)}^o(x) + \varepsilon \hat{u}_{(1)}^o(x), \\ \hat{u}^i(\xi; \theta_2, \theta_4, \theta_5) &= \hat{u}_{(0)}^i(\xi) + \varepsilon \{ \xi \hat{u}_{(c)}^i(\xi) + \hat{u}_{(1)}^i(\xi) \}.\end{aligned}$$

Remark 2. The network $\hat{u}_{(c)}^i(\xi)$ is introduced to enforce consistency between the inner and outer approximations under Van Dyke's matching principle. Since $\xi = \frac{x-x_0}{\varepsilon}$, it follows that $x = \varepsilon\xi + x_0$, and hence the term $\varepsilon\xi\hat{u}_{(c)}^i(\xi)$ can be rewritten as $(x-x_0)\hat{u}_{(c)}^i(\xi)$. This implies that although $\hat{u}_{(c)}^i(\xi)$ appears as part of the first-order expansion, it contributes to the zeroth-order behavior. Such design is crucial for realizing Van Dyke's matching principle, aligning the asymptotic orders between the inner and outer expansions.

Based on Van Dyke's matching principle and our construction, we propose the following theorem:

Theorem 1. We consider five independent neural networks: $\hat{u}_{(0)}^o(x; \theta_1) : \Omega_o \times \Theta \rightarrow \mathbb{R}$ representing the leading-order outer approximation network, $\hat{u}_{(0)}^i(\xi; \theta_2) : \Omega'_i \times \Theta \rightarrow \mathbb{R}$ representing the leading-order inner approximation network, $\hat{u}_{(1)}^o(x; \theta_3) : \Omega_o \times \Theta \rightarrow \mathbb{R}$ representing the first-order outer approximation network, $\hat{u}_{(c)}^i(\xi; \theta_4) : \Omega'_i \times \Theta \rightarrow \mathbb{R}$ representing the order-reduction network, and $\hat{u}_{(1)}^i(\xi; \theta_5) : \Omega'_i \times \Theta \rightarrow \mathbb{R}$ representing the first-order inner approximation network. Here, Θ denotes the parameter space of the neural networks. The Van Dyke's matching condition for the neural networks is

$$\hat{u}_{(0)}^o(x_0; \theta_1) = \hat{u}_{(0)}^i(+\infty; \theta_2), \quad \hat{u}_{(1)}^o(x_0; \theta_3) = \hat{u}_{(1)}^i(+\infty; \theta_5), \quad [\hat{u}_{(0)}^o]'(x_0; \theta_1) = \hat{u}_{(c)}^i(+\infty; \theta_4),$$

where $[\hat{u}_{(0)}^o]'$ denotes the derivative of $\hat{u}_{(0)}^o$ with respect to x .

For the detailed proof of this theorem, see the Appendix A.

The neural networks' parameters $\theta = \{\theta_1, \theta_2, \theta_3, \theta_4, \theta_5\}$ are optimized by the following loss function:

$$\mathcal{L}(\theta; \mathcal{T}) = \mathcal{L}^o(\theta_1, \theta_3; \mathcal{T}_o) + \mathcal{L}^i(\theta_2, \theta_4, \theta_5; \mathcal{T}_i) + \mathcal{L}^m(\theta_1, \theta_2, \theta_3, \theta_4, \theta_5; \mathcal{T}_m) + \mathcal{L}^b(\theta_1, \theta_2, \theta_3, \theta_4, \theta_5; \mathcal{T}_b), \quad (10)$$

where

$$\mathcal{L}^o(\theta_1, \theta_3; \mathcal{T}_o) = \frac{1}{|\mathcal{T}_o|} \sum_{x \in \mathcal{T}_o} \left(\left| \mathcal{F}_0(\hat{u}_{(0)}^o, x) \right|^2 + \left| \mathcal{F}_1(\hat{u}_{(0)}^o, \hat{u}_{(1)}^o, x) \right|^2 \right), \quad (11)$$

$$\mathcal{L}^i(\theta_2, \theta_4, \theta_5; \mathcal{T}_i) = \frac{1}{|\mathcal{T}_i|} \sum_{x \in \mathcal{T}_i} \left| \tilde{\mathcal{F}}(\hat{u}^i, \xi, \varepsilon) \right|^2, \quad (12)$$

$$\mathcal{L}^m(\theta_1, \theta_2, \theta_3, \theta_4, \theta_5; \mathcal{T}_m) = \left| \hat{u}_{(0)}^o(x_0) - \hat{u}_{(0)}^i(\xi_0) \right|^2 + \left| \hat{u}_{(1)}^o(x_0) - \hat{u}_{(1)}^i(\xi_0) \right|^2 + \left| [\hat{u}_{(0)}^o]'(x_0) - \hat{u}_{(c)}^i(\xi_0) \right|^2, \quad (13)$$

$$\mathcal{L}^b(\theta_1, \theta_2, \theta_3, \theta_4, \theta_5; \mathcal{T}_b) = \frac{1}{|\Gamma^o|} \sum_{x \in \Gamma^o} |\mathcal{B}^o(\hat{u}^o, \varepsilon)|^2 + \frac{1}{|\Gamma^i|} \sum_{\xi \in \Gamma^i} |\mathcal{B}^i(\hat{u}^i, \varepsilon)|^2. \quad (14)$$

Remark 3. From the perspective of well-posedness, the inner and outer approximations require different treatments in the loss design. The outer expansions $\hat{u}_{(0)}^o$ and $\hat{u}_{(1)}^o$ correspond to separate orders of the original governing equation posed on the outer domain, where each order often admits a well-defined boundary value problem. Thus, it is both natural and mathematically justified to impose separate residual losses \mathcal{F}_0 and \mathcal{F}_1

for the leading and first-order outer approximations. In contrast, the inner asymptotic expansion terms $\hat{u}_{(0)}^i$, $\hat{u}_{(1)}^i$ and $\hat{u}_{(c)}^i$ do not form well-posed problems on their own. To ensure well-posedness and stable training, we treat the inner approximation as a unified whole and define the residual loss based on the transformed equation $\tilde{\mathcal{F}}(u^i, \xi, \varepsilon)$. This approach constrains all inner components simultaneously while preserving the structure of the asymptotic expansion.

Finally, we construct the composite solution in the form:

$$\hat{u}(x; \theta) = \hat{u}^o(x) + \hat{u}^i \left(\frac{x - x_0}{\varepsilon} \right) - \hat{u}_{(1)}^{o,i}, \quad x \in \Omega, \quad (15)$$

where $\hat{u}_{(1)}^{o,i} = \hat{u}_{(0)}^i(\xi_0) + \hat{u}_{(c)}^i(\xi_0)(x - x_0) + \varepsilon \hat{u}_{(1)}^i(\xi_0)$ is the Van Dyke matching term. Following the same strategy as described in leading-order PVD-Net, the inner and outer solutions are extended across Ω , and the overlapping contribution is removed by the matching term. The implementation of the proposed high-order PVD-Net is outlined in Algorithm 2.

Algorithm 2 High-order PVD-Net

- 1: **Input:** Outer residual points \mathcal{T}_o , inner residual points \mathcal{T}_i , matching points \mathcal{T}_m , boundary residual points \mathcal{T}_b , learning rate η , total iterations N_{iter} .
 - 2: **Output:** The trainable parameters θ , the composite solution $\hat{u}(x; \theta)$.
 - 3: Initialize five neural networks $\hat{u}_{(0)}^o(x; \theta_1)$, $\hat{u}_{(0)}^i(\xi; \theta_2)$, $\hat{u}_{(1)}^o(x; \theta_3)$, $\hat{u}_{(c)}^i(\xi; \theta_4)$, $\hat{u}_{(1)}^i(\xi; \theta_5)$;
 - 4: **for** $iter = 1$ to N_{iter} **do**
 - 5: Compute equation losses \mathcal{L}^o , \mathcal{L}^i , \mathcal{L}^m , \mathcal{L}^b as defined in (11)–(14);
 - 6: Compute total loss $\mathcal{L}(\theta; \mathcal{T})$ as given in (10);
 - 7: Simultaneously update each neural network’s parameters using gradient descent $\theta \leftarrow \theta - \eta \nabla_{\theta} \mathcal{L}$;
 - 8: **end for**
 - 9: Compute composite solution $\hat{u}(x; \theta)$ as given in (15);
 - 10: **Return** trained parameters θ ; composite solution $\hat{u}(x; \theta)$.
-

3.2. Prandtl-Van Dyke Deep Operator Network (PVD-ONet)

In this section, we describe the PVD-ONet framework. The framework further extends the applicability of PVD-Net by using operator learning techniques, and PVD-ONet is capable of learning solutions across a family of boundary layer problems. We still provide both leading-order and high-order approximation. The leading-order approximation ensures acceptable accuracy and maintains computational efficiency, making it suitable for scenarios where stability and simplicity are prioritized. The high-order approximation improves precision by capturing finer details of the solution, making it ideal for applications requiring higher accuracy.

3.2.1. Physics-informed DeepONet

The DeepONet [48] is a powerful framework for learning solution operators of entire families of PDEs. Let \mathcal{V} denotes the input function space, typically containing initial conditions, boundary conditions, or other parameters, and let \mathcal{U} denotes the solution space of the corresponding PDEs. We consider a general family of parametric partial differential equations of the form

$$\mathcal{N}(v, u) = 0,$$

where $v \in \mathcal{V}$ denotes the input function, and $u \in \mathcal{U}$ denotes the corresponding solution of the system. The goal is to learn the solution operator $G_\theta : \mathcal{V} \rightarrow \mathcal{U}$, which maps each input $v \in \mathcal{V}$ to its associated solution $u = G_\theta(v) \in \mathcal{U}$. To represent v numerically, it is necessary to discretize it using a set of “sensor points” $\{x_1, x_2, \dots, x_M\} \subset \Omega$. The function v is then approximated by its point-wise evaluations at these sensor points:

$$\mathbf{v} = [v(x_1), v(x_2), \dots, v(x_M)] \in \mathbb{R}^M,$$

where \mathbf{v} is the finite-dimensional representation of v . The DeepONet consists of two main sub-networks: the “branch” network and the “trunk” network. The discretized input v is fed into the branch network, which encodes it into a finite-dimensional feature vector. The trunk network takes the coordinate $\zeta \in \Omega$ as input. Finally, the output of the DeepONet is denoted as

$$G_\theta(v)(\zeta) := \sum_{i=1}^p b_i(\mathbf{v}) \cdot t_i(\zeta),$$

where b_1, b_2, \dots, b_p is the output of the branch network, t_1, t_2, \dots, t_p is the output of the trunk network.

Building upon the original DeepONet framework, Physics-informed DeepONet [52] further integrates physical knowledge in the loss function. Specifically, the loss function is defined as follows:

$$\mathcal{L} = \frac{1}{NJM} \sum_{n=1}^N \sum_{j=1}^J \sum_{m=1}^M |\mathcal{N}(v_n(x_m), G_\theta(v_n)(\zeta_{n,j}))|^2,$$

where $\{v_n\}_{n=1}^N \subset \mathcal{V}$ are input functions sampled from the input space, for each n , $\{\zeta_{n,j}\}_{j=1}^J$ denotes a set of collocation points sampled within the domain where $G_\theta(v_n)$ is defined. $\{x_m\}_{m=1}^M$ represents a fixed set of sensor points used to evaluate the input functions. The overall architecture of the Physics-informed DeepONet is depicted in Figure 4.

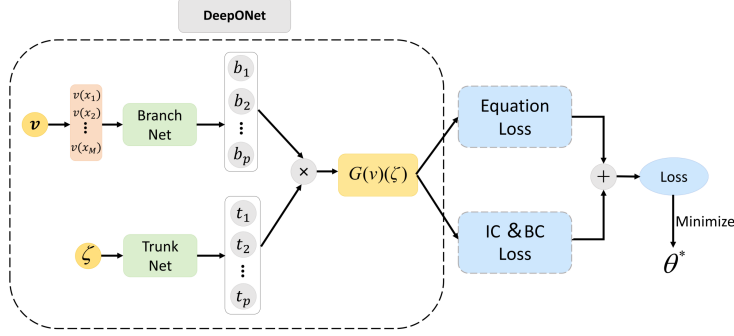


Figure 4: The architecture of Physics-informed DeepONet. The network consists of a branch network that encodes the input function v sampled at fixed sensor locations $\{x_1, x_2, \dots, x_M\}$, and a trunk network that takes coordinate ζ as input. The outputs of the two networks are combined by dot product to approximate the solution operator. Automatic differentiation is used to compute PDE residuals and enforce physical constraints.

3.2.2. Leading-order PVD-ONet

In this subsection, we extend the leading-order PVD-Net framework to the operator learning setting by incorporating the DeepONet architecture. The inner and outer networks, denoted as $G_{(0)}^o : \mathcal{V} \rightarrow \mathcal{U}$ and $G_{(0)}^i : \mathcal{V} \rightarrow \mathcal{U}$, are parameterized using DeepONets with parameters θ_1 and θ_2 , respectively. They are designed to approximate the inner solution and outer solution of the parametric boundary layer problem. The Prandtl matching principle remains essentially the same as leading-order PVD-Net, is expressed as

$$\lim_{x \rightarrow x_0} G_{(0)}^o(v)(x) = \lim_{\xi \rightarrow \infty} G_{(0)}^i(v)(\xi), \quad v \in \mathcal{V}.$$

The loss function for the leading-order PVD-ONet is structured similarly to the leading-order PVD-Net. Specifically, for $\theta = \{\theta_1, \theta_2\}$, the loss function is defined as follows:

$$\mathcal{L}(\theta; \mathcal{T}) := \mathcal{L}^o(\theta_1; \mathcal{T}_o) + \mathcal{L}^i(\theta_2; \mathcal{T}_i) + \mathcal{L}^m(\theta_1, \theta_2; \mathcal{T}_m) + \mathcal{L}^b(\theta_1, \theta_2; \mathcal{T}_b), \quad (16)$$

where

$$\mathcal{L}^o(\theta_1; \mathcal{T}_o) = \frac{1}{N|\mathcal{T}_o|} \sum_{n=1}^N \sum_{x \in \mathcal{T}_o} \left| \mathcal{F}_0(G_{(0)}^o(v_n), x) \right|^2, \quad (17)$$

$$\mathcal{L}^i(\theta_2; \mathcal{T}_i) = \frac{1}{N|\mathcal{T}_i|} \sum_{n=1}^N \sum_{\xi \in \mathcal{T}_i} \left| \tilde{\mathcal{F}}_0(G_{(0)}^i(v_n), \xi) \right|^2, \quad (18)$$

$$\mathcal{L}^m(\theta_1, \theta_2; \mathcal{T}_m) = \frac{1}{N} \sum_{n=1}^N \left| G_{(0)}^o(v_n)(x_o) - G_{(0)}^i(v_n)(\xi_0) \right|^2, \quad (19)$$

$$\mathcal{L}^b(\theta_1, \theta_2; \mathcal{T}_b) = \frac{1}{N|\Gamma^o|} \sum_{n=1}^N \sum_{x \in \Gamma^o} \left| \mathcal{B}^o(G_{(0)}^o(v_n), \varepsilon) \right|^2 + \frac{1}{N|\Gamma^i|} \sum_{n=1}^N \sum_{\xi \in \Gamma^i} \left| \mathcal{B}^i(G_{(0)}^i(v_n), \varepsilon) \right|^2. \quad (20)$$

The composite solution for the uniformly valid approximation is given by:

$$G(v_n)(x; \theta) = G_{(0)}^o(v_n)(x) + G_{(0)}^i(v_n) \left(\frac{x - x_0}{\varepsilon} \right) - G_{(0)}^{o,i}(v_n), \quad x \in \Omega, \quad (21)$$

where $G_{(0)}^{o,i}(v_n) = G_{(0)}^o(v_n)(x_0)$ (or $G_{(0)}^i(v_n)(\xi_0)$) is the Prandtl matching term. Algorithm 3 provides the pseudo code for the implementation of the proposed leading-order PVD-ONet.

Algorithm 3 Leading-order PVD-ONet

- 1: **Input:** Outer residual points \mathcal{T}_o , inner residual points \mathcal{T}_i , matching points \mathcal{T}_m , boundary residual points \mathcal{T}_b , learning rate η , total iterations N_{iter} , input functions $\{v_n\}_{n=1}^N$.
 - 2: **Output:** The trainable parameters θ , the composite solution $G(v_n)(x; \theta)$.
 - 3: Initialize outer DeepONet $G_{(0)}^o$ with parameter θ_1 and inner DeepONet $G_{(0)}^i$ with parameter θ_2 .
 - 4: **for** $iter = 1$ to N_{iter} **do**
 - 5: Compute losses $\mathcal{L}^o, \mathcal{L}^i, \mathcal{L}^m, \mathcal{L}^b$ as defined in (17)–(20);
 - 6: Compute total loss $\mathcal{L}(\theta; \mathcal{T})$ as given in (16);
 - 7: Simultaneously update parameters of both networks using gradient descent $\theta \leftarrow \theta - \eta \nabla_{\theta} \mathcal{L}$;
 - 8: **end for**
 - 9: Compute composite solution $G(v_n)(x; \theta)$ as given in (21);
 - 10: **Return** trained parameters θ ; composite solution $G(v_n)(x; \theta)$.
-

3.2.3. High-order PVD-ONet

We extend the high-order PVD-Net framework by incorporating the DeepONet architecture to enable operator learning. As a result, both the outer and inner solutions are now approximated through DeepONet. Specifically, analogous to the definitions of the high-order PVD-Net, $G_{(0)}^o : \mathcal{V} \rightarrow \mathcal{U}$ and $G_{(0)}^i : \mathcal{V} \rightarrow \mathcal{U}$, parameterized by θ_1 and θ_2 , respectively, represent the zeroth-order operator approximations. The first-order operator approximations are modeled by $G_{(1)}^o : \mathcal{V} \rightarrow \mathcal{U}$, $G_{(c)}^i : \mathcal{V} \rightarrow \mathcal{U}$ and $G_{(1)}^i : \mathcal{V} \rightarrow \mathcal{U}$ with corresponding parameters θ_3, θ_4 and θ_5 . We propose a novel operator-learning-based framework for constructing two-term asymptotic expansions of both the inner and outer solutions, which can be expressed as:

$$\begin{aligned} G^o(v)(x; \theta_1, \theta_3) &= G_{(0)}^o(v)(x) + \varepsilon G_{(1)}^o(v)(x), \\ G^i(v)(\xi; \theta_2, \theta_4, \theta_5) &= G_{(0)}^i(v)(\xi) + \varepsilon \{ \xi G_{(c)}^i(v)(\xi) + G_{(1)}^i(v)(\xi) \}. \end{aligned}$$

Similar to the high-order PVD-Net's setting, the neural networks' parameters $\theta = \{\theta_1, \theta_2, \theta_3, \theta_4, \theta_5\}$ are optimized by the following loss function:

$$\mathcal{L}(\theta; \mathcal{T}) = \mathcal{L}^o(\theta_1, \theta_3; \mathcal{T}_o) + \mathcal{L}^i(\theta_2, \theta_4, \theta_5; \mathcal{T}_i) + \mathcal{L}^m(\theta_1, \theta_2, \theta_3, \theta_4, \theta_5; \mathcal{T}_m) + \mathcal{L}^b(\theta_1, \theta_2, \theta_3, \theta_4, \theta_5; \mathcal{T}_b), \quad (22)$$

where

$$\mathcal{L}^o(\theta_1, \theta_3; \mathcal{T}_o) = \frac{1}{N|\mathcal{T}_o|} \sum_{n=1}^N \sum_{x \in \mathcal{T}_o} \left(\left| \mathcal{F}_0(G_{(0)}^o(v_n), x) \right|^2 + \left| \mathcal{F}_1(G_{(0)}^o(v_n), G_{(1)}^o(v_n), x) \right|^2 \right), \quad (23)$$

$$\mathcal{L}^i(\theta_2, \theta_4, \theta_5; \mathcal{T}_i) = \frac{1}{N|\mathcal{T}_i|} \sum_{n=1}^N \sum_{x \in \mathcal{T}_i} \left| \tilde{\mathcal{F}}(G^i(v_n), \xi, \varepsilon) \right|^2, \quad (24)$$

$$\begin{aligned} \mathcal{L}^m(\theta_1, \theta_2, \theta_3, \theta_4, \theta_5; \mathcal{T}_m) = & \frac{1}{N} \sum_{n=1}^N \left(\left| G_{(0)}^o(v_n)(x_0) - G_{(0)}^i(v_n)(\xi_0) \right|^2 + \left| G_{(1)}^o(v_n)(x_0) - G_{(1)}^i(v_n)(\xi_0) \right|^2 \right. \\ & \left. + \left| [G_{(0)}^o(v_n)]'(x_0) - G_{(c)}^i(v_n)(\xi_0) \right|^2 \right), \end{aligned} \quad (25)$$

$$\mathcal{L}^b(\theta_1, \theta_2, \theta_3, \theta_4, \theta_5; \mathcal{T}_b) = \frac{1}{N|\Gamma^o|} \sum_{n=1}^N \sum_{x \in \Gamma^o} |\mathcal{B}^o(G^o(v_n), \varepsilon)|^2 + \frac{1}{N|\Gamma^i|} \sum_{n=1}^N \sum_{\xi \in \Gamma^i} |\mathcal{B}^i(G^i(v_n), \varepsilon)|^2. \quad (26)$$

Finally, the composite solution is constructed as:

$$G(v_n)(x; \theta) = G^o(v_n)(x) + G^i(v_n) \left(\frac{x - x_o}{\varepsilon} \right) - G_{(1)}^{o,i}(v_n), \quad x \in \Omega, \quad (27)$$

where $G_{(1)}^{o,i}(v_n) = G_{(0)}^i(v_n)(\xi_0) + G_{(c)}^i(v_n)(\xi_0)(x - x_0) + \varepsilon G_{(1)}^i(v_n)(\xi_0)$. A detailed algorithm for the proposed high-order PVD-ONet is presented in Algorithm 4. The structure of the PVD-ONet is shown in Figure 5.

Algorithm 4 High-Order PVD-ONet

- 1: **Input:** Outer residual points \mathcal{T}_o , inner residual points \mathcal{T}_i , matching points \mathcal{T}_v , boundary residual points \mathcal{T}_b , learning rate η , total iterations N_{iter} , input functions $\{v_n\}_{n=1}^N$.
 - 2: **Output:** The trainable parameters θ , the composite solution $G(v_n)(x; \theta)$.
 - 3: Initialize networks $G_{(0)}^o$, $G_{(0)}^i$, $G_{(1)}^o$, $G_{(c)}^i$, $G_{(1)}^i$ with parameters $\theta_1, \theta_2, \theta_3, \theta_4, \theta_5$, respectively;
 - 4: **for** $iter = 1$ to N_{iter} **do**
 - 5: Compute equation losses \mathcal{L}^o , \mathcal{L}^i , \mathcal{L}^v , \mathcal{L}^b as defined in (23)–(26);
 - 6: Compute total loss $\mathcal{L}(\theta; \mathcal{T})$ as given in (22);
 - 7: Simultaneously update each neural network's parameters using gradient descent $\theta \leftarrow \theta - \eta \nabla_{\theta} \mathcal{L}$.
 - 8: **end for**
 - 9: Compute composite solution $G(v_n)(x; \theta)$ as given by (27);
 - 10: **Return** trained parameters θ ; composite solution $G(v_n)(x; \theta)$.
-

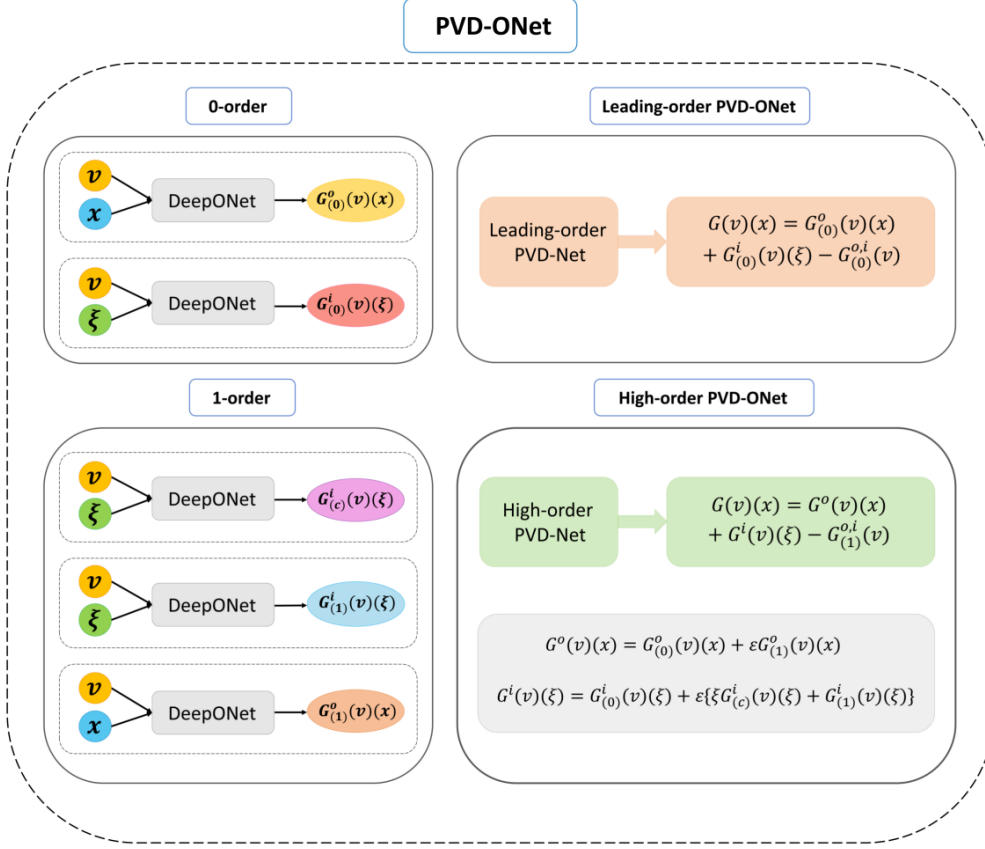


Figure 5: The architecture of PVD-ONet. Similar to PVD-Net, PVD-ONet also consists of two approximation versions. PVD-ONet adopts DeepONet—a more expressive framework for operator learning. For the leading-order PVD-ONet, the model comprises two networks—an inner and an outer network—that learn a family of boundary layer problems. In contrast, the high-order PVD-ONet employs five networks to capture finer-scale structures.

4. Numerical experiments

In this section, we illustrate the effectiveness of our proposed PVD-Net and PVD-ONet through numerical experiments. Moreover, for each example, PVD-Net is compared with MSM-NNs [44] as well as BL-PINNs [39] to demonstrate the superiority of our approach. PVD-ONet is compared with Physics-informed DeepONet [52] to demonstrate the effectiveness of our framework. We use the Adam optimizer combined with Glorot initialization, and the SiLU activation function is employed in all the experiments. For all experiments, we train for 100,000 iterations and select the best-performing model during training for evaluation. To ensure a fair comparison, all methods used the same total number of neurons and were trained and tested under the same conditions. Specifically, all methods employ 5 hidden layers with 100 neurons per layer (consisting of two neural networks), except for the high-order PVD-Net and PVD-ONet (consisting of five neural networks), which use 5 hidden layers with 40 neurons per layer, ensuring that the

total number of neurons remains the same for each method. Since computers are incapable of handling infinity, we employ a sufficiently large finite value $\xi_0 = 20$ to approximate the concept of infinity. All the experiments are performed on NVIDIA RTX A6000 48GB GPU.

4.1. Accuracy Evaluation Metrics

To evaluate and compare the performance of our method with existing approaches, we introduced multiple accuracy metrics. Through a systematic and fair comparison of these metrics, we are able to comprehensively quantify the performance differences among various methods. Focusing on the boundary layer inner—where fluid-solid interaction and viscous effects are most significant—we densely sampled 10,000 points in this region to compute the inner relative L^2 and L^∞ errors. Additionally, we measured errors at the inner-outer junction point, a region prone to sharp gradients and predictive instability, to assess model generalization and numerical accuracy. This not only reveals the generalization behavior of the model, but also provides an important assessment of the numerical solution accuracy of the boundary layer problem. To ensure the comprehensiveness of the metrics, we also sampled 100 points in the outer region of the boundary layer. The combined sampling strategy yields 10,101 discrete evaluation points (10,000 inner + 100 outer + 1 critical junction point). Based on these data, we calculated the global relative L^2 error and L^∞ error.

4.2. Second-order equation with constant coefficients

Let us consider a second-order equation with constant coefficients presented in

$$\begin{cases} \varepsilon \frac{d^2 u}{dx^2} + \frac{du}{dx} + u = 0, & x \in (0, 1), \\ u(0) = \alpha, & u(1) = \beta, \end{cases} \quad (28)$$

where $\varepsilon = 10^{-3}$, $\alpha = 1$ and $\beta = 2$. Equation (28) has an analytical solution given by

$$u = \frac{-\alpha e^{\lambda_2} + \beta}{e^{\lambda_1} - e^{\lambda_2}} e^{\lambda_1 x} + \frac{\alpha e^{\lambda_1} - \beta}{e^{\lambda_1} - e^{\lambda_2}} e^{\lambda_2 x}, \quad (29)$$

where $\lambda_1 = \frac{-1 + \sqrt{1 - 4\varepsilon}}{2\varepsilon}$, $\lambda_2 = \frac{-1 - \sqrt{1 - 4\varepsilon}}{2\varepsilon}$. This equation represents a fundamental problem in the theory of singular perturbations [10]. Despite its simple form, it captures the essential features of singular perturbation behavior, such as multiscale dynamics and boundary layer formation, and thus serves as a prototype for numerical method development. The small coefficients in this equation are multiplied by the highest order derivatives of the equation, hence the boundary layer phenomenon occurs. In this example, the boundary layer is at $x = 0$, and an inner expansion using the stretching transformation $\xi = \frac{x}{\varepsilon}$ was introduced to amplify the boundary layer. A detailed analysis of this example is provided in the Appendix B, where the coefficients are set as $a(x) = 1$, $b(x) = 1$.

PVD-Net. Since the governing equation is known, it is straightforward to derive the equations at different orders via asymptotic expansion (see Appendix B). For both the boundary layer and outer regions, we uniformly sample 200 training points within each region to construct the sets \mathcal{T}_i and \mathcal{T}_o , respectively. For the leading-order PVD-Net, loss functions (5)-(8) can be written in the following explicit forms:

$$\mathcal{L}^o(\theta_1; \mathcal{T}_o) = \frac{1}{|\mathcal{T}_o|} \sum_{x \in \mathcal{T}_o} \left| \frac{d\hat{u}_{(0)}^o}{dx} + \hat{u}_{(0)}^o \right|^2,$$

$$\mathcal{L}^i(\theta_2; \mathcal{T}_i) = \frac{1}{|\mathcal{T}_i|} \sum_{\xi \in \mathcal{T}_i} \left| \frac{d^2 \hat{u}_{(0)}^i}{d\xi^2} + \frac{d\hat{u}_{(0)}^i}{d\xi} \right|^2,$$

$$\mathcal{L}^m(\theta_1, \theta_2; \mathcal{T}_m) = \left| \hat{u}_{(0)}^o(0) - \hat{u}_{(0)}^i(\xi_0) \right|^2,$$

$$\mathcal{L}^b(\theta_1, \theta_2; \mathcal{T}_b) = \left| \hat{u}_{(0)}^i(0) - \alpha \right|^2 + \left| \hat{u}_{(0)}^o(1) - \beta \right|^2.$$

For the high-order PVD-Net, the explicit formulations of the loss functions (11)–(14) are given below:

$$\mathcal{L}^o(\theta_1, \theta_3; \mathcal{T}_o) = \frac{1}{|\mathcal{T}_o|} \sum_{x \in \mathcal{T}_o} \left(\left| \frac{d\hat{u}_{(0)}^o}{dx} + \hat{u}_{(0)}^o \right|^2 + \left| \frac{d\hat{u}_{(1)}^o}{dx} + \hat{u}_{(1)}^o + \frac{d^2 \hat{u}_{(0)}^o}{dx^2} \right|^2 \right),$$

$$\mathcal{L}^i(\theta_2, \theta_4, \theta_5; \mathcal{T}_i) = \frac{1}{|\mathcal{T}_i|} \sum_{x \in \mathcal{T}_i} \left| \frac{d^2 \hat{u}^i}{d\xi^2} + \frac{d\hat{u}^i}{d\xi} + \varepsilon \hat{u}^i \right|^2,$$

$$\mathcal{L}^m(\theta_1, \theta_2, \theta_3, \theta_4, \theta_5; \mathcal{T}_m) = \left| \hat{u}_{(0)}^o(0) - \hat{u}_{(0)}^i(\xi_0) \right|^2 + \left| \hat{u}_{(1)}^o(0) - \hat{u}_{(1)}^i(\xi_0) \right|^2 + \left| [\hat{u}_{(0)}^o]'(0) - \hat{u}_{(c)}^i(\xi_0) \right|^2,$$

$$\mathcal{L}^b(\theta_1, \theta_2, \theta_3, \theta_4, \theta_5; \mathcal{T}_b) = \left| \hat{u}_{(1)}^o(1) - 0 \right|^2 + \left| \hat{u}_{(0)}^o(1) - \beta \right|^2 + \left| \hat{u}_{(1)}^i(0) - 0 \right|^2 + \left| \hat{u}_{(0)}^i(0) - \alpha \right|^2.$$

The prediction results of our method are shown in Figure 6. From the figure, it can be confirmed that our proposed PVD-Net framework is able to solve the boundary layer problem efficiently, and its predicted solution maintains good smoothness in the computational domain. It is particularly remarkable that the higher-order version exhibits better numerical accuracy compared with the leading-order version, and this advantage is especially significant in the boundary layer gradient change region. Table 2 demonstrates a comparison of the prediction errors of the different methods in the boundary layer problem. It can be observed from the systematic error analysis that the high-order PVD-Net method exhibits the best numerical performance under all metrics. Our leading-order PVD-Net demonstrates consistent improvements over BL-PINNs across all evaluation metrics. Comparative analysis reveals that while MSM-NN achieves comparable performance in terms of relative L^2 error, our method maintains a distinct advantage in L^∞ error. This result indicates that our method has higher accuracy and reliability in capturing boundary layer problems and provides a more effective numerical tool for solving such problems.

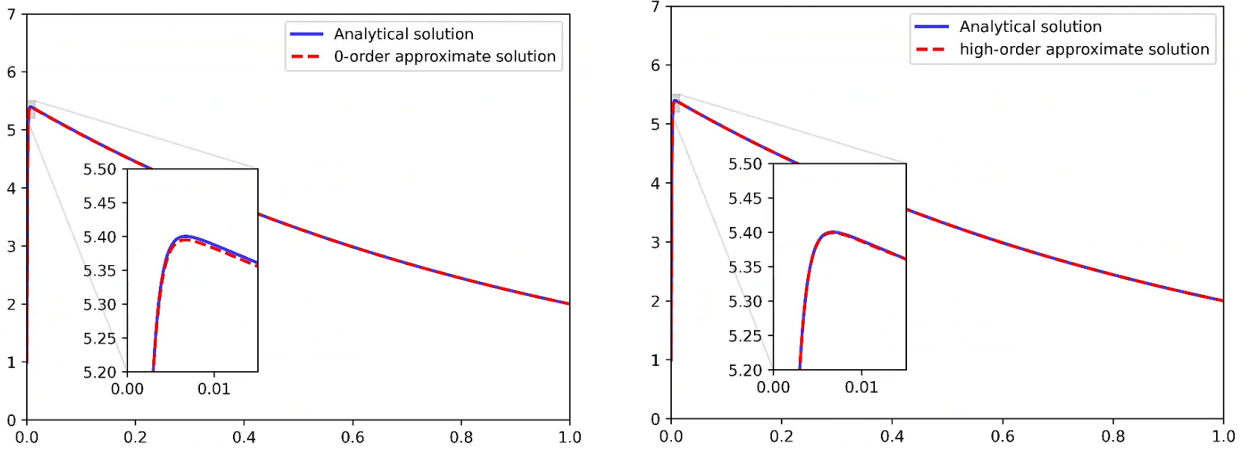


Figure 6: **(Left):** Predicted results of Leading-order PVD-Net. **(Right):** Predicted results of High-order PVD-Net. As can be seen from the above panels, our proposed PVD-Net is able to efficiently learn the solutions of the boundary layer problem, and the differences between the analytic and real solutions are almost indistinguishable, while these solutions exhibit smooth transitions. It is particularly notable that the higher-order PVD-Net exhibits significant accuracy improvement over the leading-order PVD-Net, especially in the boundary layer region and at the transition interface.

Data-driven method. We first use a purely data-driven approach for solving boundary layer problems by employing two separate DeepONet to learn the inner and outer solutions, respectively. The inner branch network input is $(a, b) = \{(a_k, b_k)\}_{k=1}^K$ and the trunk network input is ξ . The outer branch network input is $(a, b) = \{(a_k, b_k)\}_{k=1}^K$ and the trunk network input is x . We choose 1000 boundary conditions for training and 100 boundary conditions for testing. In both inner and outer regions, we use 100 observation points to supervise the learning. The results of the prediction are shown in Figure 7. The mean L^∞ prediction error is 2.2×10^{-4} .

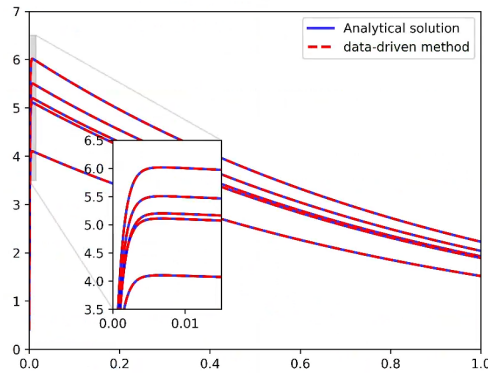


Figure 7: Assuming the location of the boundary layer is known, we separately employ DeepONets to learn the inner and outer solution operators. Specifically, we aim to learn the mapping $G : (a, b) \mapsto u$. During training, 100 observation points are sampled from both the inner and outer regions. The resulting predictions show excellent agreement with the ground truth—visually, the differences are nearly indistinguishable. Quantitatively, the mean L^∞ prediction error is 2.2×10^{-4} .

Although the data-driven method is capable of learning a family of boundary layer problems, the method suffers from a notable limitation: it requires sampling a sufficiently large number of measurements within the boundary layer to train the network effectively. However, in practice, the boundary layer is often extremely thin. For example, in high Reynolds number flows over an airfoil, the thickness of the boundary layer can be on the order of millimeters or less. This makes direct data acquisition inside the boundary layer extremely challenging, as it demands high-resolution sensors and precise experimental setups. As a result, obtaining accurate and dense measurements within the boundary layer is often impractical, which limits the applicability and robustness of the method in real-world scenarios.

PVD-ONet. For PVD-ONet, we learn a solution operator $G : (a, b) \mapsto u$ that maps boundary conditions to corresponding solutions, where the boundary parameters (a, b) are uniformly sampled from $a \sim \mathcal{U}(0.4, 1.4)$, $b \sim \mathcal{U}(1.5, 2.5)$ and u denotes the solution. We choose 1000 boundary conditions for training and 100 boundary conditions for testing. It is worth noting that PVD-ONet relies solely on the governing equations, without requiring any additional observational data for training the neural network. In a manner similar to the PVD-Net, the loss function can be rewritten in an analogous form. The prediction results are shown in Figure 8. The predicted solutions demonstrate excellent agreement with the ground truth and maintain smooth transitions across the entire domain. Notably, the high-order PVD-ONet achieves improved accuracy over the leading-order PVD-ONet, particularly in regions with sharp gradients such as the boundary layer interface. Table 3 presents a comparison of the prediction errors obtained by different methods. The results demonstrate that our approach exceeds the performance of PI-DeepONet, and the higher-order PVD-ONet provides even greater accuracy.

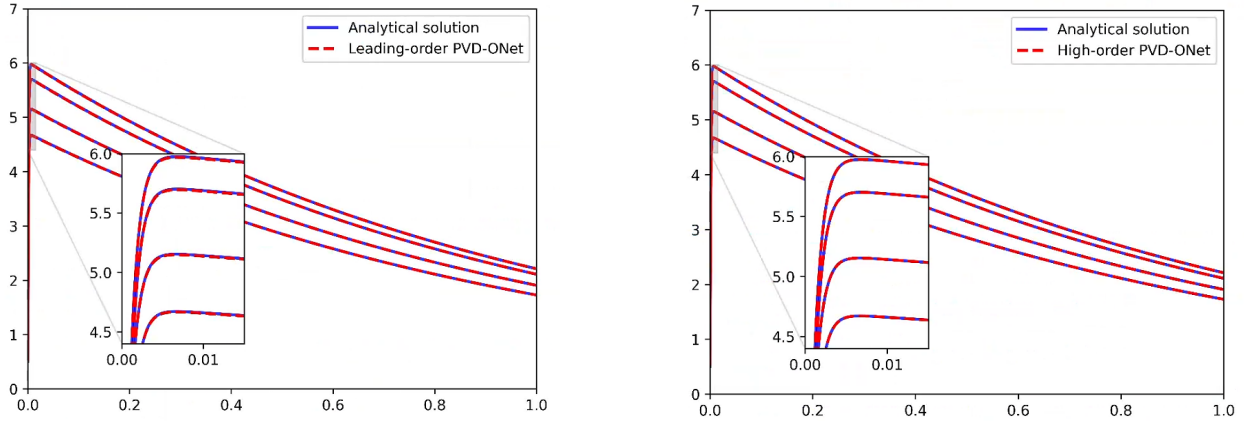


Figure 8: **(Left):** Predicted results of Leading-order PVD-ONet. **(Right):** Predicted results of High-order PVD-ONet. We aim to learn the operator $G : (a, b) \mapsto u$. As shown, the proposed PVD-ONet is capable of accurately learning the mapping from parameters to solutions in boundary layer problems. The predicted solutions closely match the ground truth, exhibiting smooth transitions. This proves that our proposed framework is able to efficiently learn the solution of a family of boundary layer problems.

4.3. Second-order equation with variable coefficients

Let us consider a second-order equation with variable coefficients presented in

$$\begin{cases} \varepsilon \frac{d^2 u}{dx^2} + a(x) \frac{du}{dx} + b(x)u = 0, & x \in (0, 1), \\ u(0) = \alpha, & u(1) = \beta, \end{cases} \quad (30)$$

where $\varepsilon = 10^{-3}$, $\alpha = 1$, $\beta = 2$, $a(x)$ and $b(x)$ are analytic functions on the interval $[0, 1]$. According to boundary layer theory [10], when $a(x) > 0$, the boundary layer is at $x = 0$. When $a(x) < 0$, the boundary layer is at $x = 1$. In our setup, we set $a(x) = x + 1$, $b(x) = 5\cos(5x)$. Since the equations (30) do not have an analytical solution, we use the finite difference method to obtain the numerical solution. The detailed procedures are provided in Appendix Appendix B.

PVD-Net. For the leading-order PVD-Net, loss functions (5)-(8) can be written in the following explicit forms:

$$\mathcal{L}^o(\theta_1; \mathcal{T}_o) = \frac{1}{|\mathcal{T}_o|} \sum_{x \in \mathcal{T}_o} \left| a(x) \frac{d\hat{u}_{(0)}^o}{dx} + b(x)\hat{u}_{(0)}^o \right|^2,$$

$$\mathcal{L}^i(\theta_2; \mathcal{T}_i) = \frac{1}{|\mathcal{T}_i|} \sum_{\xi \in \mathcal{T}_i} \left| \frac{d^2 \hat{u}_{(0)}^i}{d\xi^2} + a(0) \frac{d\hat{u}_{(0)}^i}{d\xi} \right|^2,$$

$$\mathcal{L}^m(\theta_1, \theta_2; \mathcal{T}_m) = \left| \hat{u}_{(0)}^o(0) - \hat{u}_{(0)}^i(\xi_0) \right|^2,$$

$$\mathcal{L}^b(\theta_1, \theta_2; \mathcal{T}_b) = \left| \hat{u}_{(0)}^i(0) - \alpha \right|^2 + \left| \hat{u}_{(0)}^o(1) - \beta \right|^2.$$

For the high-order PVD-Net, the explicit formulations of the loss functions (11)–(14) are given below:

$$\mathcal{L}^o(\theta_1, \theta_3; \mathcal{T}_o) = \frac{1}{|\mathcal{T}_o|} \sum_{x \in \mathcal{T}_o} \left(\left| a(x) \frac{d\hat{u}_{(0)}^o}{dx} + b(x)\hat{u}_{(0)}^o \right|^2 + \left| a(x) \frac{d\hat{u}_{(1)}^o}{dx} + b(x)\hat{u}_{(1)}^o + \frac{d^2 \hat{u}_{(0)}^o}{dx^2} \right|^2 \right),$$

$$\mathcal{L}^i(\theta_2, \theta_4, \theta_5; \mathcal{T}_i) = \frac{1}{|\mathcal{T}_i|} \sum_{x \in \mathcal{T}_i} \left| \frac{d^2 \hat{u}^i}{d\xi^2} + a(\varepsilon\xi) \frac{d\hat{u}^i}{d\xi} + \varepsilon b(\varepsilon\xi) \hat{u}^i \right|^2,$$

$$\mathcal{L}^m(\theta_1, \theta_2, \theta_3, \theta_4, \theta_5; \mathcal{T}_m) = \left| \hat{u}_{(0)}^o(0) - \hat{u}_{(0)}^i(\xi_0) \right|^2 + \left| \hat{u}_{(1)}^o(0) - \hat{u}_{(1)}^i(\xi_0) \right|^2 + \left| [\hat{u}_{(0)}^o]'(0) - \hat{u}_{(c)}^i(\xi_0) \right|^2,$$

$$\mathcal{L}^b(\theta_1, \theta_2, \theta_3, \theta_4, \theta_5; \mathcal{T}_b) = \left| \hat{u}_{(1)}^o(1) - 0 \right|^2 + \left| \hat{u}_{(0)}^o(1) - \beta \right|^2 + \left| \hat{u}_{(1)}^i(0) - 0 \right|^2 + \left| \hat{u}_{(0)}^i(0) - \alpha \right|^2.$$

The prediction results are shown in Figure 9. The numerical results demonstrate that the PVD-Net framework successfully resolves the variable-coefficient boundary layer problem across different approximation orders. Both the leading-order and high-order approximate solution that closely match the reference solution, with their prediction curves nearly overlapping the ground truth. The figure reveals that while both versions maintain smooth flow transitions, the high-order PVD-Net achieves superior boundary layer resolution. This improved accuracy makes it particularly effective for multiscale problems requiring precise boundary layer capture. As shown in Table 2, our high-order PVD-Net outperforms all baseline methods, achieving the lowest errors across all metrics. While the leading-order PVD-Net matches the accuracy of BL-PINNs—demonstrating its capability in learning multiscale problem—our approach surpasses MSM-NN, particularly in L^∞ error and junction point error. This highlights the superior precision and robustness of our framework in handling boundary layer problems with variable coefficients.

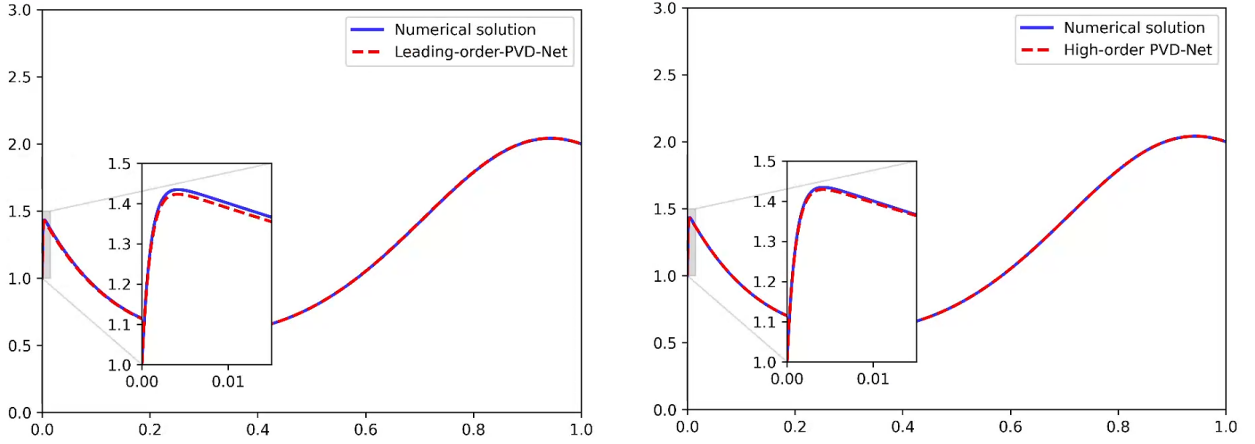


Figure 9: Prediction results of the PVD-Net for the second-order differential equation with variable coefficients. **(Left):** Predicted results of Leading-order PVD-Net. **(Right):** Predicted results of High-order PVD-Net. It can be observed that both the leading-order and high-order PVD-Net accurately capture the solution of the boundary layer problem with variable coefficients. The predicted results are virtually indistinguishable from the reference solutions, demonstrating excellent agreement. Moreover, both versions exhibit smooth transitions across the domain. A closer examination through localized zoom-in plots reveals that the high-order PVD-Net achieves superior accuracy within the boundary layer region. These results indicate that the proposed approach effectively handles multiscale problems, with the high-order PVD-Net offering enhanced precision.

PVD-ONet. Similar to the constant coefficient case, the boundary conditions (a, b) are sampled uniformly from the intervals $a \sim \mathcal{U}(0.4, 1.4)$ and $b \sim \mathcal{U}(1.5, 2.5)$. We utilize 1000 boundary conditions for training and 100 for testing. The prediction results are shown in Figure 10. The numerical results demonstrate that both leading-order and high-order PVD-ONet successfully resolve the variable-coefficient boundary layer problem, with predicted solution showing excellent agreement with reference solution. As we can see by the localized zoomed-in view, the higher-order version is able to learn the solution more accurately. Table 3 presents a detailed comparison of the prediction errors obtained from various methods. The results clearly

show that our approach outperforms PI-DeepONet, with the higher-order PVD-ONet delivering even better accuracy.

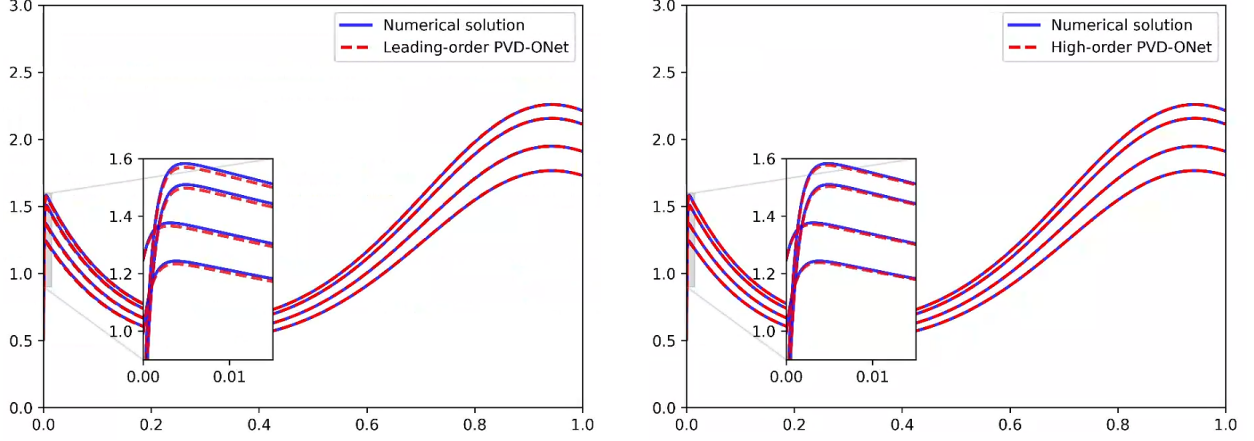


Figure 10: PVD-ONet for the second-order differential equation with variable coefficients. **(Left)**: Predicted results of Leading-order PVD-ONet. **(Right)**: Predicted results of High-order PVD-ONet. Our object is to learn the operator $G : (a, b) \mapsto u$. Both models successfully capture the solution behavior, including the abrupt change near the boundary layer. Notably, the high-order version demonstrates improved accuracy, especially in regions with rapid changes, as it better resolves fine-scale structures. This highlights the effectiveness of the proposed PVD-ONet in handling a family of multiscale problem.

Table 2: Comparison of prediction errors for PVD-Net. The bolded values indicate the lowest errors among all methods.

Problem	Method	Global Errors		Inner Region Errors		Junction Point Error
		Relative L^2	L^∞	Relative L^2	L^∞	
Constant-coefficient	BL-PINNs [39]	1.50×10^{-3}	2.27×10^{-2}	1.50×10^{-3}	2.27×10^{-2}	2.21×10^{-2}
	MSM-NN [44]	5.54×10^{-4}	8.94×10^{-3}	5.55×10^{-4}	8.94×10^{-3}	3.03×10^{-4}
	Leading-order PVD-Net	9.43×10^{-4}	5.39×10^{-3}	9.44×10^{-4}	5.39×10^{-3}	5.20×10^{-3}
	High-order PVD-Net	1.44×10^{-4}	1.90×10^{-3}	1.44×10^{-4}	1.90×10^{-3}	1.02×10^{-4}
Variable-coefficient	BL-PINNs [39]	7.09×10^{-3}	1.15×10^{-2}	7.12×10^{-3}	1.15×10^{-2}	1.03×10^{-2}
	MSM-NN [44]	6.06×10^{-3}	2.21×10^{-2}	6.09×10^{-3}	2.21×10^{-2}	1.80×10^{-2}
	Leading-order PVD-Net	8.04×10^{-3}	1.19×10^{-2}	8.07×10^{-3}	1.19×10^{-2}	1.11×10^{-2}
	High-order PVD-Net	2.69×10^{-3}	5.25×10^{-3}	2.70×10^{-3}	5.25×10^{-3}	5.12×10^{-3}

5. Conclusion and Future Work

In this work, we proposed two novel frameworks, PVD-Net and PVD-ONet, for solving boundary layer problems. Inspired by the classical method of matched asymptotic expansions, we designed both leading-order and high-order approximations for PVD-Net and PVD-ONet, based on the Prandtl and Van Dyke matching principles, respectively. In the leading-order approximation, two neural networks (either fully

Table 3: Comparison of mean prediction errors for PVD-ONet. Bold indicates the lowest error among all methods.

Problem	Method	Global Errors		Inner Region Errors	
		Relative L^2	L^∞	Relative L^2	L^∞
Constant-coefficient	PI-DeepONet [52]	8.71×10^{-1}	4.80×10^0	8.71×10^{-1}	4.80×10^0
	Leading-order PVD-ONet	1.01×10^{-3}	5.83×10^{-3}	1.01×10^{-3}	5.83×10^{-3}
	High-order PVD-ONet	1.5×10^{-4}	1.82×10^{-3}	1.5×10^{-4}	1.82×10^{-3}
Variable-coefficient	PI-DeepONet [52]	3.88×10^{-1}	6.30×10^{-1}	3.89×10^{-1}	5.96×10^{-1}
	Leading-order PVD-ONet	7.78×10^{-3}	1.18×10^{-2}	7.81×10^{-3}	1.18×10^{-2}
	High-order PVD-ONet	3.34×10^{-3}	6.60×10^{-3}	3.35×10^{-3}	6.59×10^{-3}

connected network or DeepONet) are used to approximate the inner and outer solutions, which are then connected via the Prandtl matching condition—making this approach particularly suitable for stability-prioritized scenarios. In the high-order approximation, five neural networks (either fully connected network or DeepONet) are employed along with Van Dyke’s matching to capture more refined structures in the boundary layer, significantly enhancing the overall solution accuracy—making it especially effective in precision-critical scenarios. In both leading- and high-order approximations, uniformly valid composite solutions are introduced to ensure continuity. We validated our methods on both constant- and variable-coefficient differential equations. The experimental results consistently show that our proposed frameworks outperform existing baselines, demonstrating their effectiveness and robustness.

For future research, we identify several promising directions. First, we aim to develop adaptive mechanisms capable of automatically identifying the location of boundary layers based on problem-specific features, which would further enhance the flexibility and efficiency of our proposed frameworks. Second, a rigorous theoretical investigation into the approximation errors and convergence properties of both PVD-Net and PVD-ONet is planned. Such studies will provide a deeper understanding of the reliability and limitations of deep learning approaches. Finally, we intend to extend our methodologies to more complex scenarios, including high-dimensional PDEs, time-dependent problems, and systems with coupled multi-scale dynamics, thereby exploring the broader applicability of our approach in real-world scientific and engineering problems.

CRediT authorship contribution statement

Tiantian Sun: Writing – Original Draft, Editing, Code, Visualization. **Jian Zu:** Writing – Review and Editing, Code, Data Analysis, Validation, Supervision, Methodology.

Declaration of competing interest

The authors declare that they have no known competing financial interests or personal relationships that could have appeared to influence the work reported in this paper.

Data availability

Data will be made available on request.

Acknowledgements

J. Zu gratefully acknowledges the financial support from the Science and Technology Development Plan Project of Jilin Province (No. 20250102016JC).

Appendix A. Proof of Theorem 1

Proof. Consider the outer solution \hat{u}^o expressed in terms of the outer variable x , expanded up to first order as:

$$\hat{u}^o(x) = \hat{u}_{(0)}^o(x) + \varepsilon \hat{u}_{(1)}^o(x), \quad (\text{A.1})$$

where $\hat{u}_{(0)}^o(x)$ and $\hat{u}_{(1)}^o(x)$ denote the leading-order and first-order outer approximations represented by neural networks, respectively. To analyze its behavior in the inner region, we rewrite it using the inner variable $\xi = \frac{x-x_0}{\varepsilon}$. Substituting $x = \varepsilon\xi + x_0$ into the (A.1), we obtain:

$$[\hat{u}^o]^i = \hat{u}_{(0)}^o(\varepsilon\xi + x_0) + \varepsilon \hat{u}_{(1)}^o(\varepsilon\xi + x_0).$$

Expanding $\hat{u}_{(0)}^o(\varepsilon\xi + x_0)$ and $\hat{u}_{(1)}^o(\varepsilon\xi + x_0)$ using Taylor series around $\varepsilon\xi + x_0 = x_0$, we have:

$$\hat{u}_{(0)}^o(\varepsilon\xi + x_0) = \hat{u}_{(0)}^o(x_0) + [\hat{u}_{(0)}^o]'(x_0)(\varepsilon\xi) + \frac{1}{2}[\hat{u}_{(0)}^o]''(x_0)(\varepsilon\xi)^2 + \dots,$$

$$\hat{u}_{(1)}^o(\varepsilon\xi + x_0) = \hat{u}_{(1)}^o(x_0) + [\hat{u}_{(1)}^o]'(x_0)(\varepsilon\xi) + \frac{1}{2}[\hat{u}_{(1)}^o]''(x_0)(\varepsilon\xi)^2 + \dots$$

Substituting these expansions into $[\hat{u}^o]^i$, we obtain

$$[\hat{u}^o]^i = (\hat{u}_{(0)}^o(x_0) + [\hat{u}_{(0)}^o]'(x_0)(\varepsilon\xi) + \dots) + \varepsilon(\hat{u}_{(1)}^o(x_0) + [\hat{u}_{(1)}^o]'(x_0)(\varepsilon\xi) + \dots).$$

Retaining terms up to $O(\varepsilon)$, the two-term inner expansion of the outer solution is:

$$[\hat{u}^o]^i = \hat{u}_{(0)}^o(x_0) + [\hat{u}_{(0)}^o]'(x_0)(x - x_0) + \varepsilon \hat{u}_{(1)}^o(x_0).$$

Similarly, consider the inner solution \hat{u}^i expressed in terms of the inner variable ξ , and expand it up to first order in ε :

$$\hat{u}^i = \hat{u}_{(0)}^i(\xi) + \varepsilon\{\hat{u}_{(1)}^i(\xi) + \hat{u}_{(c)}^i(\xi)\xi\}, \quad (\text{A.2})$$

where $\hat{u}_{(0)}^i(\xi)$ denotes the leading-order inner approximation network, $\hat{u}_{(1)}^i(\xi)$ denotes the first-order outer approximation network and $\hat{u}_{(c)}^i(\xi)$ represents the order-reduction network. To analyze its behavior in the outer region, we rewrite it using the outer variable $x = \varepsilon\xi + x_0$. Substituting $\xi = \frac{x-x_0}{\varepsilon}$ into (A.2), we obtain:

$$[\hat{u}^i]^o = \hat{u}_{(0)}^i\left(\frac{x-x_0}{\varepsilon}\right) + \varepsilon\left\{\hat{u}_{(1)}^i\left(\frac{x-x_0}{\varepsilon}\right) + \hat{u}_{(c)}^i\left(\frac{x-x_0}{\varepsilon}\right)\frac{x-x_0}{\varepsilon}\right\}.$$

For fixed x , let $\varepsilon \rightarrow 0$, then we have

$$\hat{u}_{(0)}^i\left(\frac{x-x_0}{\varepsilon}\right) \rightarrow \hat{u}_{(0)}^i(+\infty), \quad \hat{u}_{(c)}^i\left(\frac{x-x_0}{\varepsilon}\right) \rightarrow \hat{u}_{(c)}^i(+\infty), \quad \hat{u}_{(1)}^i\left(\frac{x-x_0}{\varepsilon}\right) \rightarrow \hat{u}_{(1)}^i(+\infty).$$

Thus, we obtain the two-term outer expansion of the inner solution:

$$[\hat{u}^i]^o = \hat{u}_{(0)}^i(+\infty) + \hat{u}_{(c)}^i(+\infty)(x-x_0) + \varepsilon\hat{u}_{(1)}^i(+\infty).$$

According to Van Dyke's matching principle, The two-term inner expansion of the two-term outer expansion is equal to the two-term outer expansion of the two-term inner expansion. This leads to the following equality:

$$\hat{u}_{(0)}^o(x_0) + [\hat{u}_{(0)}^o]'(x_0)(x-x_0) + \varepsilon\hat{u}_{(1)}^o(x_0) = \hat{u}_{(0)}^i(+\infty) + \hat{u}_{(c)}^i(+\infty)(x-x_0) + \varepsilon\hat{u}_{(1)}^i(+\infty).$$

For this equality to hold for all x and ξ , the corresponding coefficients must match. This yields the Van Dyke matching conditions for the neural network approximations:

$$\hat{u}_{(0)}^o(x_0) = \hat{u}_{(0)}^i(+\infty), \quad \hat{u}_{(1)}^o(x_0) = \hat{u}_{(1)}^i(+\infty), \quad [\hat{u}_{(0)}^o]'(x_0) = \hat{u}_{(c)}^i(+\infty).$$

□

Appendix B. Second-order equation with variable coefficients

Consider a second-order equation with variable coefficients presented in

$$\begin{cases} \varepsilon \frac{d^2 u}{dx^2} + a(x) \frac{du}{dx} + b(x)u = 0, & x \in (0, 1), \\ u(0) = \alpha, & u(1) = \beta. \end{cases} \quad (\text{B.1})$$

When $a(x) > 0$, the boundary layer is located at $x = 0$.

For the outer region, let $\varepsilon \rightarrow 0$, the equation (B.1) degenerates to

$$a(x) \frac{du^o}{dx} + b(x)u^o = 0, \quad (\text{B.2})$$

which is a first order differential equation that cannot simultaneously satisfy two boundary conditions. Therefore we have to discard one of the boundary conditions. From equation (B.2), the second order derivative term $\varepsilon \frac{d^2 u^o}{dx^2}$ is neglected. This means that the solutions of the equations are dominated by the first order equations in the outer region. In order to match the outer solution, the boundary condition at $x = 0$ is usually discarded, while the boundary condition at $x = 1$ is retained. Hence, (B.1) becomes

$$\begin{cases} a(x) \frac{du^o}{dx} + b(x)u^o = 0, \\ u^o(1) = \beta. \end{cases}$$

For the inner of the boundary layer, the second order derivative term $\varepsilon \frac{d^2 u}{dx^2}$ becomes important and cannot be neglected. To accurately capture the behavior within the boundary layer, the stretching transformation $\xi = \frac{x}{\varepsilon}$ is introduced, (B.1) becomes

$$\frac{d^2 u^i}{d\xi^2} + a(\varepsilon\xi) \frac{du^i}{d\xi} + \varepsilon b(\varepsilon\xi)u^i = 0.$$

Let $\varepsilon \rightarrow 0$, we have

$$\frac{d^2 u^i}{d\xi^2} + a(0) \frac{du^i}{d\xi} = 0.$$

Inside the boundary layer, the the boundary condition at $x = 0$ is retained. Therefore, we have

$$\begin{cases} \frac{d^2 u^i}{d\xi^2} + a(0) \frac{du^i}{d\xi} = 0, \\ u^i(0) = \alpha. \end{cases}$$

For high-order matching of variable-coefficient boundary layer problems, we consider an asymptotic expansion of the outer solution in the form

$$u^o(x) = \sum_{n=0}^{m-1} \varepsilon^n \varphi_n(x) + O(\varepsilon^m).$$

By substituting the expansion into the governing equation given in (B.1) and equating terms of like powers of ε , we obtain the following hierarchy of equations:

$$\begin{aligned} \varepsilon^0 : \quad & a(x) \frac{d\varphi_0}{dx} + b(x)\varphi_0(x) = 0, \\ \varepsilon^n : \quad & a(x) \frac{d\varphi_n}{dx} + b(x)\varphi_n(x) = -\frac{d^2 \varphi_{n-1}}{dx^2}, \quad n = 1, 2, \dots, m. \end{aligned}$$

As with the standard matched asymptotic expansion approach, the outer solution is expected to be accurate throughout the domain except within the boundary layer near $x = 0$. Therefore, it satisfies the outer boundary condition at $x = 1$, so it satisfies the boundary condition $u^o(1) = \beta$, which yields

$$\varphi_0(1) = \beta, \quad \varphi_n(1) = 0, \quad n = 1, 2, \dots, m.$$

For the inner expansion, first use the stretching transformation $\xi = \frac{x}{\varepsilon}$ to change equation (B.1) into

$$\frac{d^2 u}{d\xi^2} + a(\varepsilon\xi) \frac{du}{d\xi} + \varepsilon b(\varepsilon\xi)u = 0. \quad (\text{B.3})$$

The asymptotic expansion of the inner solution is defined as follows:

$$u^i(\xi) = \sum_{n=0}^{m-1} \varepsilon^n \psi_n(\xi) + O(\varepsilon^m).$$

Substituting the expansion into the governing equation (B.3) and collecting terms with the same powers of ε , we derive the following hierarchy of equations:

$$\begin{aligned} \varepsilon^0 : \quad & \frac{d^2 \psi_0}{d\xi^2} + a(\varepsilon\xi) \frac{d\psi_0}{d\xi} = 0, \\ \varepsilon^n : \quad & \frac{d^2 \psi_n}{d\xi^2} + a(\varepsilon\xi) \frac{d\psi_n}{d\xi} = -b(\varepsilon\xi) \psi_{n-1}, \quad n = 1, 2, \dots, m. \end{aligned}$$

Similar to the previous discussion, the boundary condition $u^i(0) = \alpha$ is retained, i.e.,

$$\psi_0(0) = \alpha, \quad \psi_n(0) = 0, \quad n = 1, 2, \dots, m.$$

References

- [1] F. M. White, J. Majdalani, Viscous fluid flow, Vol. 3, McGraw-Hill New York, 2006.
- [2] F. M. White, Fluid mechanics 8th edition (2017).
- [3] W. Schoppa, F. Hussain, A large-scale control strategy for drag reduction in turbulent boundary layers, *Physics of Fluids* 10 (5) (1998) 1049–1051. doi:<https://doi.org/10.1063/1.869789>.
- [4] J. D. Anderson, Hypersonic and high temperature gas dynamics, AIAA, 1989.
- [5] J. Anderson, Fundamentals of Aerodynamics, McGraw Hill, 2011.
- [6] E. L. Reiss, Symmetric bending of thick circular plates, *Journal of the Society for Industrial and Applied Mathematics* 10 (4) (1962) 596–609. doi:<https://doi.org/10.1137/0110045>.
- [7] W.-Z. Chien, Large deflection of a circular clamped plate under uniform pressure, *Chinese Journal of Physics* 7 (2) (1947) 102–113.
- [8] W. E. Alzheimer, R. Davis, Unsymmetrical bending of prestressed annular plates, *Journal of the Engineering Mechanics Division* 94 (4) (1968) 905–918. doi:<https://doi.org/10.1061/JMCEA3.0001000>.
- [9] A. Arzani, A. M. Gambaruto, G. Chen, S. C. Shadden, Lagrangian wall shear stress structures and near-wall transport in high-schmidt-number aneurysmal flows, *Journal of Fluid Mechanics* 790 (2016) 158–172. doi:<https://doi.org/10.1017/jfm.2016.6>.
- [10] A. H. Nayfeh, Perturbation methods, John Wiley & Sons, 2024.
- [11] L. Prandtl, On fluid motions with very small friction, *Verhldg* 3 (1904) 484–491.
- [12] T. Von Kármán, Über laminare und turbulente reibung, *Z. Angew. Math. Mech.* 1 (1921) 233–252. doi:<https://doi.org/10.1002/zamm.19210010401>.
- [13] M. Van Dyke, Higher approximations in boundary-layer theory part 1. general analysis, *Journal of Fluid Mechanics* 14 (2) (1962) 161–177. doi:<https://doi.org/10.1017/S0022112062001147>.
- [14] M. Van Dyke, Higher approximations in boundary-layer theory part 2. application to leading edges, *Journal of Fluid Mechanics* 14 (4) (1962) 481–495. doi:<https://doi.org/10.1017/S0022112062001391>.

- [15] M. Van Dyke, Higher approximations in boundary-layer theory part 3. parabola in uniform stream, *Journal of Fluid Mechanics* 19 (1) (1964) 145–159. doi:<https://doi.org/10.1017/S002211206400060X>.
- [16] R. E. O'Malley, A boundary value problem for certain nonlinear second order differential equations with a small parameter, *Archive for Rational Mechanics and Analysis* 29 (1968) 66–74.
- [17] R. E. O'Malley, Topics in singular perturbations, *Advances in Mathematics* 2 (4) (1968) 365–470. doi:[https://doi.org/10.1016/0001-8708\(68\)90023-6](https://doi.org/10.1016/0001-8708(68)90023-6).
- [18] R. E. O'Malley, Boundary value problems for linear systems of ordinary differential equations involving many small parameters, *Journal of Mathematics and Mechanics* 18 (9) (1969) 835–855.
- [19] R. E. O'Malley, Boundary layer methods for nonlinear initial value problems, *SIAM Review* 13 (4) (1971) 425–434. doi:<https://doi.org/10.1137/1013091>.
- [20] A. H. Nayfeh, A generalized method for treating singular perturbation problems, Stanford University, 1964.
- [21] A. H. Nayfeh, A comparison of three perturbation methods for earth-moon-spaceship problem, *AIAA Journal* 3 (9) (1965) 1682–1687. doi:<https://doi.org/10.2514/3.3226>.
- [22] A. H. Nayfeh, A perturbation method for treating nonlinear oscillation problems, *Journal of Mathematics and Physics* 44 (1-4) (1965) 368–374. doi:<https://doi.org/10.1002/sapm1965441368>.
- [23] T. J. Hughes, The finite element method: linear static and dynamic finite element analysis, Courier Corporation, 2012.
- [24] R. Eymard, T. Gallouët, R. Herbin, Finite volume methods, *Handbook of Numerical Analysis* 7 (2000) 713–1018. doi:[https://doi.org/10.1016/S1570-8659\(00\)07005-8](https://doi.org/10.1016/S1570-8659(00)07005-8).
- [25] J. C. Strikwerda, Finite difference schemes and partial differential equations, SIAM, 2004.
- [26] J. Ling, A. Kurzawski, J. Templeton, Reynolds averaged turbulence modelling using deep neural networks with embedded invariance, *Journal of Fluid Mechanics* 807 (2016) 155–166. doi:<https://doi.org/10.1017/jfm.2016.615>.
- [27] P. A. Srinivasan, L. Guastoni, H. Azizpour, P. Schlatter, R. Vinuesa, Predictions of turbulent shear flows using deep neural networks, *Physical Review Fluids* 4 (5) (2019) 054603. doi:<https://doi.org/10.1103/PhysRevFluids.4.054603>.
- [28] C. Jiang, R. Vinuesa, R. Chen, J. Mi, S. Laima, H. Li, An interpretable framework of data-driven turbulence modeling using deep neural networks, *Physics of Fluids* 33 (5) (2021) 055133. doi:<https://doi.org/10.1063/5.0048909>.
- [29] S. L. Brunton, B. R. Noack, P. Koumoutsakos, Machine learning for fluid mechanics, *Annual Review of Fluid Mechanics* 52 (1) (2020) 477–508. doi:<https://doi.org/10.1146/annurev-fluid-010719-060214>.
- [30] M. Raissi, P. Perdikaris, G. E. Karniadakis, Physics-informed neural networks: A deep learning framework for solving forward and inverse problems involving nonlinear partial differential equations, *Journal of Computational Physics* 378 (2019) 686–707. doi:<https://doi.org/10.1016/j.jcp.2018.10.045>.
- [31] L. Lu, X. Meng, Z. Mao, G. E. Karniadakis, DeepXDE: A deep learning library for solving differential equations, *SIAM Review* 63 (1) (2021) 208–228. doi:<https://doi.org/10.1137/19M1274067>.
- [32] A. Arzani, J.-X. Wang, R. M. D'Souza, Uncovering near-wall blood flow from sparse data with physics-informed neural networks, *Physics of Fluids* 33 (7) (2021) 071905. doi:<https://doi.org/10.1063/5.0055600>.
- [33] W. Ji, W. Qiu, Z. Shi, S. Pan, S. Deng, Stiff-pinn: Physics-informed neural network for stiff chemical kinetics, *The Journal of Physical Chemistry A* 125 (36) (2021) 8098–8106. doi:<https://pubs.acs.org/doi/10.1021/acs.jpca.1c05102>.
- [34] S. Cai, Z. Mao, Z. Wang, M. Yin, G. E. Karniadakis, Physics-informed neural networks (PINNs) for fluid mechanics: A review, *Acta Mechanica Sinica* 37 (12) (2021) 1727–1738.
- [35] Z. Mao, A. D. Jagtap, G. E. Karniadakis, Physics-informed neural networks for high-speed flows, *Computer Methods in Applied Mechanics and Engineering* 360 (2020) 112789. doi:<https://doi.org/10.1016/j.cma.2019.112789>.
- [36] C. Rao, H. Sun, Y. Liu, Physics-informed deep learning for incompressible laminar flows, *Theoretical and Applied Mechanics Letters* 10 (3) (2020) 207–212. doi:<https://doi.org/10.1016/j.taml.2020.01.039>.
- [37] K. Shukla, A. D. Jagtap, J. L. Blackshire, D. Sparkman, G. E. Karniadakis, A physics-informed neural network for

- quantifying the microstructural properties of polycrystalline nickel using ultrasound data: A promising approach for solving inverse problems, *IEEE Signal Processing Magazine* 39 (1) (2021) 68–77. doi:10.1109/MSP.2021.3118904.
- [38] G. E. Karniadakis, I. G. Kevrekidis, L. Lu, P. Perdikaris, S. Wang, L. Yang, Physics-informed machine learning, *Nature Reviews Physics* 3 (6) (2021) 422–440.
- [39] A. Arzani, K. W. Cassel, R. M. D’Souza, Theory-guided physics-informed neural networks for boundary layer problems with singular perturbation, *Journal of Computational Physics* 473 (2023) 111768. doi:https://doi.org/10.1016/j.jcp.2022.111768.
- [40] A. D. Jagtap, G. E. Karniadakis, Extended physics-informed neural networks (XPINNs): A generalized space-time domain decomposition based deep learning framework for nonlinear partial differential equations, *Communications in Computational Physics* 28 (5) (2020) 2002–2041. doi:https://doi.org/10.4208/cicp.oa-2020-0164.
- [41] M. A. Nabian, R. J. Gladstone, H. Meidani, Efficient training of physics-informed neural networks via importance sampling, *Computer-Aided Civil and Infrastructure Engineering* 36 (8) (2021) 962–977. doi:https://doi.org/10.1111/mice.12685.
- [42] S. Wang, H. Wang, P. Perdikaris, On the eigenvector bias of Fourier feature networks: From regression to solving multi-scale PDEs with physics-informed neural networks, *Computer Methods in Applied Mechanics and Engineering* 384 (2021) 113938. doi:https://doi.org/10.1016/j.cma.2021.113938.
- [43] S. Kaplun, P. A. Lagerstrom, L. N. Howard, C.-s. Liu, *Fluid Mechanics and Singular Perturbations: A Collection of Papers*, Academic Press, New York/London, 1967.
- [44] L. Zhang, G. He, Multi-scale-matching neural networks for thin plate bending problem, *Theoretical and Applied Mechanics Letters* 14 (1) (2024) 100494. doi:https://doi.org/10.1016/j.taml.2024.100494.
- [45] F. Cao, F. Gao, X. Guo, D. Yuan, Physics-informed neural networks with parameter asymptotic strategy for learning singularly perturbed convection-dominated problem, *Computers & Mathematics with Applications* 150 (2023) 229–242. doi:https://doi.org/10.1016/j.camwa.2023.09.030.
- [46] J. Huang, R. Qiu, J. Wang, Y. Wang, Multi-scale physics-informed neural networks for solving high reynolds number boundary layer flows based on matched asymptotic expansions, *Theoretical and Applied Mechanics Letters* 14 (2) (2024) 100496. doi:https://doi.org/10.1016/j.taml.2024.100496.
- [47] Z. Li, N. Kovachki, K. Azizzadenesheli, B. Liu, K. Bhattacharya, A. Stuart, A. Anandkumar, Neural operator: Graph kernel network for partial differential equations (2020). arXiv:2003.03485.
- [48] L. Lu, P. Jin, G. Pang, Z. Zhang, G. E. Karniadakis, Learning nonlinear operators via DeepONet based on the universal approximation theorem of operators, *Nature Machine Intelligence* 3 (3) (2021) 218–229.
- [49] Z. Li, N. Kovachki, K. Azizzadenesheli, B. Liu, K. Bhattacharya, A. Stuart, A. Anandkumar, Fourier neural operator for parametric partial differential equations (2020). arXiv:2010.08895.
- [50] N. Kovachki, Z. Li, B. Liu, K. Azizzadenesheli, K. Bhattacharya, A. Stuart, A. Anandkumar, Neural operator: Learning maps between function spaces with applications to PDEs, *Journal of Machine Learning Research* 24 (89) (2023) 1–97.
- [51] T. Du, Z. Huang, Y. Li, Approximation and generalization of DeepONets for learning operators arising from a class of singularly perturbed problems (2023). arXiv:2306.16833.
- [52] S. Wang, H. Wang, P. Perdikaris, Learning the solution operator of parametric partial differential equations with physics-informed DeepONets, *Science Advances* 7 (40) (2021) eabi8605. doi:10.1126/sciadv.abi8605.
- [53] A. Erdélyi, An expansion procedure for singular perturbations, *Atti Accad. Sci. Torino Cl. Sci. Fis. Mat. Nat.*, 1961.
- [54] A. G. Baydin, B. A. Pearlmutter, A. A. Radul, J. M. Siskind, Automatic differentiation in machine learning: a survey, *Journal of Machine Learning Research* 18 (153) (2018) 1–43.
- [55] D. P. Kingma, J. Ba, Adam: A method for stochastic optimization (2014). arXiv:1412.6980.
- [56] D. C. Liu, J. Nocedal, On the limited memory BFGS method for large scale optimization, *Mathematical Programming* 45 (1) (1989) 503–528.